On the comparison of two solid-shell formulations based on in-plane reduced and full integration schemes in linear and non-linear applications

A.BenBettaieb[1], J.l Velosa de Sena[2], R.J. Alves de Sousa[2], R.A.F. Valente[2], A.M. Habraken[1,3], L.Duchêne[1]

[1] University of Liège, Department ArGEnCo, Division MS2F Chemin des Chevreuils 1, 4000, Liège, Belgium.

[2] University of Aveiro, Department of Mechanical Engineering, Centre for Mechanical Technology and Automation (TEMA), Department of Mechanical Engineering, 3810-193 Aveiro, Portugal.

[3] The Belgian Fund for Scientific Research – FNRS

Abstract

In the present paper, a detailed description of the formulation of the new SSH3D solid-shell element is presented. This formulation is compared with the previously proposed RESS solid-shell element [1, 2]. Both elements were recently implemented within the LAGAMINE in-house research finite element code. These solid-shell elements possess eight nodes with only displacement nodal degrees of freedom (DOF). In order to overcome various locking pathologies, the SSH3D formulation employs the well known Enhanced Assumed Strain (EAS) concept originally introduced by Simo and Rifai [3] and based on the Hu-Veubeke-Washizu variational principle combined with the Assumed Natural Strain (ANS) technique based on the work of Dvorkin and Bathe [4]. For the RESS solid-shell element, on the other hand, only the EAS technique is used with a Reduced Integration (RI) Scheme. A particular characteristic of these elements is their special integration schemes, with an arbitrary number of integration points along the thickness direction, dedicated to analyze problems involving non-linear through-thickness distribution (i.e. metal forming applications) without requiring many element layers. The formulation of the SSH3D element is also particular, with regard to the solid-shell elements proposed in the literature, in the sense that it is characterized by an in-plane full integration and a large variety in terms of (i) enhancing parameters, (ii) the ANS version choice and (iii) the number of integration points through the thickness direction. The choice for these three parameters should be adapted to each problem so as to obtain accurate results and to keep the calculation time low.

Numerous numerical examples are performed to investigate the performance of these elements. These examples illustrate the reliability and the efficiency of the proposed formulations in various cases including linear and non-linear problems. SSH3D element is more robust thanks to the various options proposed and its full in-plane integration scheme, while RESS element in more efficient from a computational point of view.

KEY WORDS: Enhanced Assumed Strain, Assumed Natural Strain, Solid-shell, Stabilization technique

1 Introduction

A large number of research works were devoted to the development of low-order 3D finite elements for the modeling of thin shell structures. This is due to their efficiency in term of computational cost and their wide range of applicability in several types of mechanical analysis. In this context, several published works were focused on the development of solid-shell elements (e.g. see [5-13]) which form a class of finite element models that are intermediate between the conventional solid and shell elements. Despite their attractive features, low-order solid-shell displacement-based finite elements suffer from different types of locking effects. This phenomenon, which occurs under certain circumstances, is characterized by a severe underestimation of the element nodal displacements, i.e. the structural response is too stiff and it has "locked" itself against the deformations. The locking

phenomena can be overcome by various modifications on the low order element formulation. On the other hand, the use of high-order formulations can be effective due to their high capacity to capture the actual geometry of curved shell structures, but these formulations are very sensitive to mesh distortion. In addition to the order of the special interpolation, the integration scheme has a large effect on the occurrence of the locking phenomena and the overall performance of the element. In this context, two main integration schemes are usually used in the development of 3D eight node isoparametric finite elements: (i) full integration (FI), where eight (2x2x2) integration points located at certain particular positions within each Finite Element defined by the Gauss coordinates, are used; and (ii) reduced integration (RI), which is based on one integration point located at the element center. Both schemes have their benefits and drawbacks.

For instance, the reduced integration allows reducing significantly locking pathologies, being; in addition very attractive from the computational point of view. But, at the same time, it can lead to serious problems in the Finite Element model, such as numerical instabilities (the well-known 'hourglass phenomenon') and also convergence problems, which require the use of complicated stabilization techniques (for further details on RI schemes see [1, 14, 15]). For these reasons, full integration scheme is more frequently used for the development of 3D finite elements such as in the case of solid-shell elements (e.g. [5, 6, 16-19]) even if it suffers from several locking pathologies. In order to reduce these locking effects, several techniques are available in the literature for low-order fully integrated solid and solid-shell formulations. Among these techniques, the B-Bar and the selective reduced integration (SRI) techniques are considered as the most efficient, especially in the treatment of volumetric locking. These methods were initially proposed by Malkus et al. [20] and by Hughes [21] for shell and plate elements.

In addition to the above techniques, two very popular and effective techniques are used in the development of 3D low-order solid-shell finite elements to eliminate locking problems: The enhanced Assumed Strain (EAS) and the Assumed Natural Strain (ANS) techniques.

In 1990, Simo and Rifai present in their work [3] the first four-node finite element, for geometrically linear problems, based on the three field variational principle of Hu-Washizu which is called by 'the Enhanced Assumed Strain method'. Later, this method was extended for the analysis of non-linear problems based on the enhancement of the deformation gradient tensor F in the works of Simo and Armero [22] and Miehe [16]. The EAS procedure was also applied directly to enhance the Green-Lagrange strain tensor E in several works (e.g. Klinkel et al. [23, 24], Vu-Quoc and Tan [6, 7], Alves de Sousa et al. [1, 25], Parente et al. [26], Schwarze et al. [27], among others).

Comparing these different ways to introduce the EAS technique is not obvious. In reference [6], departing from a numerical experimentation, the authors indicate that the EAS formulation based on the Green-Lagrange strain E is more efficient than the EAS formulation based on the enhancing of the deformation gradient F like the formulation described in [16]. Additionally, according to [6], the same results are obtained with both approaches when the same EAS parameters are used.

In [28], Andelfinger and Ramm applied the Enhanced Assumed Strain for the development of a four node membrane, plate and shell elements and a 3D eight node solid element. In this reference, equivalence of some formulations based on the EAS method and Hellinger-Reissner principle is discussed.

Despite the fact that the Enhanced Assumed Strain is very attractive when it is used to overcome locking pathologies and to improve the element accuracy, it is considered as inefficient in term of computational time. Therefore, the choice of the optimal EAS parameters is a crucial matter for several published works (e.g. Betsh et al [29], Andelfinger and Ramm [28], Vu-Quoc and Tan [6], Klinkel et al. [18], Alves de Sousa et al. [25], Miehe [16], Rah et al. [12]). This choice should depend on the type of analysis for which the element is used. Unfortunately, this method has some limitations in the solving of certain particular locking pathologies, especially in the modeling of very thin

structures and in the case of mesh distortion. Therefore, another very popular technique is used in several research works in the few last decades and known as the Assumed Natural Strain (ANS) method.

The Assumed Natural Strain (ANS) method is considered among the most efficient techniques, which have been frequently used to overcome transverse shear and curvature thickness locking. This technique uses a very straightforward procedure to treat these locking pathologies, especially in bending situation. It consists in modifying the interpolation scheme of certain strain components that are plagued by locking phenomena (the transverse shear strain components E_{13} and E_{23} to tackle the transverse shear locking and the transverse normal component E_{33} to tackle the curvature thickness locking). These strain components are firstly calculated using the classical interpolation method in the element domain at the so-called 'sampling points', which are located where the parasitic strain distributions vanish. Thereafter, the calculated components are evaluated at the Gauss points using bilinear or linear interpolation functions (depending on the number of sampling points) from their values at the sampling points.

This method was originally applied for four shell elements by Dvorkin and Bathe [4] ant it has proven to be efficient, very robust and to give very good results for four node plate bending theory based on Mindlin/Reissner plate theory in [30] (applied on the transverse shear strain components E_{13}, E_{23}). This method was later extended to overcome the curvature thickness locking by modifying the interpolation of the transverse normal strain component E_{33} for four-node shell elements, as proposed by Betsch and Stein [29] and also Bischoff and Ramm [31]. In the recent development of solid-shell elements, numerous formulations are developed based on the combination of the EAS and ANS methods such as the work of Hauptman et al. [5], Miehe [16], Klinkel et al. [18], Vu-Quoc and Tan [6], Cardoso et al. [32], Schwarze and Reese [10] and the recent works of Rah et al. [12] and Pramin et al. [33].

Taking all these references and achievements in the literature, the main goal of the present paper is to present the formulations of the SSH3D (=Solid-SHell element in 3D) and RESS (=Reduced Enhanced Solid-Shell element) solid-shell elements. Then, to assess the elements for some numerical results, which were achieved thanks to the LAGAMINE in-house research finite element code, in which these elements are implemented. The code is an implicit non-linear FE program with an updated Lagrangian formulation and it is adapted to large strains and large displacements. It has been under development at the ArGEnCo department of the university of Liège since 1982 and was initiated by Cescotto in order to simulate the rolling process [34]. In addition to rolling, the code has been applied to several other forming processes, such as forging [35], continuous casting [36], deep drawing [37], incremental forming [38], and to various other applications.

The present paper is outlined as follows. In Section 2.1, the most disturbing locking phenomena which occur in solid-shell elements are briefly summarized. The different techniques used to overcome these locking pathologies are presented in Sections 2.2, 2.3, 2.4 and 2.5. Then, the numerical tests are given in Section 3 to evaluate the performance of the present formulations in linear and non-linear cases. This numerical evaluation shows the good performance of both elements. Finally some conclusions and discussions are given.

2 Formulations of the SSH3D and RESS solid-shell elements

2.1 Locking phenomena in 3D solid-shell elements and possible remedies

The most disturbing locking problems infecting low-order 3D solid-shell elements can be classified as follows:

2.1.1 Volumetric locking

This phenomenon generally occurs for nearly incompressible material behavior (e.g. elastic behavior with Poisson's ratio approaching 0.5 or elastoplastic behavior). This phenomenon is caused by missing terms in the normal strain components. Therefore, the constraint of an incompressible material cannot be fulfilled by the normal strain of a pure displacement-based formulation.

Volumetric locking is a much more serious problem than shear locking, because it cannot be avoided by refining the mesh. In addition, all the standard fully integrated finite elements will lock in the incompressible limit, and some elements show very poor performance even for Poisson's ratios as small as 0.45. Fortunately, metallic materials have Poisson's ratios around 0.3, so standard elements can be used for most linear elasticity and small strain plasticity problems (where the plastic compressibility constraint is not predominant compared to the elastic behavior). Several methods, such as the EAS, SRI and B-Bar methods, have been proposed in the literature to overcome this locking phenomenon.

2.1.2 Transverse Shear locking

In 3D elements, due to their trilinear shape functions, pure transversal bending state cannot be represented without leading to accompanying parasitic transversal shear strain. This problem can occur when the element is used in the analysis of shell structures with bending dominated loading (see Klinkel et al. [23]). For solid-shell elements, the two very popular techniques, the Enhanced Assumed Strain (EAS) and the Assumed Natural Strain (ANS), are often used to remove shear locking.

2.1.3 Curvature locking

Due to the poor approximation of the low-order interpolation functions, parasitic thickness normal strains ε_{33} are always present at a Gauss point. This effect is particularly severe when coarse meshes and strong curvatures of the shell geometry exist. This locking phenomenon can be avoided by applying the ANS method on the element's transverse normal strain ε_{33}, as proposed by Betsch and Stein [39].

More locking pathologies and their possible remedies are described in detail by Caseiro et al. [40].

2.2 Variational formulation of the EAS method

The starting point of the Enhanced Assumed Strain method is the well-known Hu-Washizu three-field variational principle which can be written in the following form:

$$\pi(\mathbf{u},\boldsymbol{\varepsilon},\boldsymbol{\sigma}) = \pi_{\text{int}}(\mathbf{u},\boldsymbol{\varepsilon},\boldsymbol{\sigma}) + \pi_{\text{ext}}(\mathbf{u}), \tag{1}$$

where the internal potential π_{int} is expressed as:

$$\pi_{\text{int}}(\mathbf{u},\boldsymbol{\varepsilon},\boldsymbol{\sigma}) = \int_{\Omega} W(\boldsymbol{\varepsilon})\mathrm{dV} + \int_{\Omega} \boldsymbol{\sigma}^{\mathrm{T}}(\nabla^{\mathrm{s}}\mathbf{u} - \boldsymbol{\varepsilon})\mathrm{dV}, \tag{2}$$

and the potential energy of external forces can be written as:

$$\pi_{\text{ext}}(\mathbf{u}) = \int_{\Omega} \rho_0 \bar{\mathbf{b}}\mathbf{u}\mathrm{dV} + \int_{\partial_\sigma\Omega} \bar{\mathbf{t}}\mathbf{u}\mathrm{dA}, \tag{3}$$

where W is the stored strain energy and $\boldsymbol{\sigma}$, $\mathbf{u}$, $\boldsymbol{\varepsilon}$ are the actual stress, displacement and strain fields respectively. Here, Ω is the volume of the studied body, $\partial_\sigma\Omega$ in (3) is its external surface where surface tractions are applied and ∇^{S} is the symmetric gradient operator. Here, $\bar{\mathbf{b}}$ and $\bar{\mathbf{t}}$ are the prescribed body forces and traction vectors, respectively. Finally, ρ_0 is the density of the material.

The variation of (1), with respect to the three independent variables $\mathbf{u}$, $\boldsymbol{\varepsilon}$ and $\boldsymbol{\sigma}$ respectively, is calculated via the so-called Gâteaux derivatives and leads to the following equations:

$$\int_\Omega \boldsymbol{\sigma}^{\mathrm{T}} \nabla^{\mathrm{s}} \delta\mathbf{u} \mathrm{dV} - \pi_{\mathrm{ext}}(\delta\mathbf{u}) = 0 \tag{4}$$

$$\int_\Omega \delta\boldsymbol{\varepsilon}^{\mathrm{T}} (\partial_\varepsilon \mathrm{W} - \boldsymbol{\sigma}) \mathrm{dV} = 0 \tag{5}$$

$$\int_\Omega \delta\boldsymbol{\sigma}^{\mathrm{T}} (\nabla^{\mathrm{s}} \mathbf{u} - \boldsymbol{\varepsilon}) \mathrm{dV} = 0 \tag{6}$$

Within the elastoplastic FE framework, $\partial_\varepsilon \mathrm{W}$ (in equation (5)) should return the stress computed by the constitutive law at material point **x** for the strains **ε**, therefore it should preferably be noted $\boldsymbol{\sigma}^{\mathrm{m}}(\mathbf{x},\boldsymbol{\varepsilon})$ where m stands for material.

The kinematic of this formulation is based only on displacement degrees of freedom (DOFs). Therefore, and relying the isoparametric concept, the standard shape functions for eight node hexahedral elements are used to approximate the position vector of the reference configuration **X** and the displacement vector **U** via the following relations:

$$\mathbf{X}_i = \sum_{k=1}^{8} \mathrm{N}_k(\xi,\eta,\zeta)\mathbf{X}_{ik} \text{ and } \mathbf{u}_i = \sum_{k=1}^{8} \mathrm{N}_k(\xi,\eta,\zeta)\mathbf{U}_{ik}, \tag{7}$$

where the index '*i*' (= 1, 2, 3) refers to the three directions of the local axes system. Also, $\mathrm{N}_k(\xi,\eta,\zeta)$ with (*k*=1 to 8) in (7) denote the shape functions defined in natural coordinate system and which can be expressed as follows:

$$\mathrm{N}_k(\xi,\eta,\zeta) = \frac{1}{8}(1+\xi_k\xi)(1+\eta_k\eta)(1+\zeta_k\zeta), \tag{8}$$

where (ξ_k, η_k, ζ_k), $\mathbf{X}_{ik}$ and $\mathbf{U}_{ik}$ denote the natural coordinates, the global nodal coordinates and the nodal displacements of node *k*, respectively. From equation (8), it can be seen that the shape functions vary linearly in the ξ, η and ζ directions. Therefore these shape functions are usually called tri-linear functions.

The aim of the EAS method is to remove the artificial stiffening of the standard eight-node displacement-based solid elements due to the low order of the shape functions. This undesirable excessive stiffness generally lead to inaccurate results in bending dominated problems as well as in modeling of nearly incompressible materials. These two problems are related to the transverse shear locking and the volumetric locking, which are considered in the present work as the major locking phenomena to be studied. These two types of locking are responsible for the low quality of the standard displacement elements.

The key idea of the EAS technique is therefore to improve the classical compatible strain field by adding the enhanced part via the following equation:

$$\boldsymbol{\varepsilon} = \boldsymbol{\varepsilon}^{\mathrm{c}} + \boldsymbol{\varepsilon}^{\alpha} = \mathbf{B}(\xi,\eta,\zeta)\mathbf{U} + \mathbf{G}(\xi,\eta,\zeta)\boldsymbol{\alpha}, \tag{9}$$

where $\boldsymbol{\varepsilon}^{\mathrm{c}}$ is the compatible strain field computed as the symmetric gradient of the interpolated displacement field **U**. Using the element nodal displacement in (7), $\boldsymbol{\varepsilon}^{\mathrm{c}}$ contains the 24 compatible modes and can be obtained thanks to the well-known strain-displacement matrix **B**.

As the shape functions N_k are defined in terms of the natural coordinates (ξ,η,ζ) to obtain the derivatives with respect to the global coordinates (x, y, z) in the strain displacement matrix **B**, a chain rule of partial differentiation needs to be used:

$$\begin{bmatrix} \dfrac{\partial \mathrm{N}_k}{\partial x} \\ \dfrac{\partial \mathrm{N}_k}{\partial y} \\ \dfrac{\partial \mathrm{N}_k}{\partial z} \end{bmatrix} = \mathbf{J}^{-1} \begin{bmatrix} \dfrac{\partial \mathrm{N}_k}{\partial \xi} \\ \dfrac{\partial \mathrm{N}_k}{\partial \eta} \\ \dfrac{\partial \mathrm{N}_k}{\partial \zeta} \end{bmatrix} \tag{10}$$

where **J** is the Jacobian matrix. This equation serves to transform the strain-displacement matrix from the element natural coordinate system to the global coordinate system. The Jacobian matrix can be defined by:

$$\mathbf{J}(\xi,\eta,\zeta)=\begin{bmatrix}\frac{\partial x}{\partial \xi} & \frac{\partial x}{\partial \eta} & \frac{\partial x}{\partial \zeta}\\ \frac{\partial y}{\partial \xi} & \frac{\partial y}{\partial \eta} & \frac{\partial y}{\partial \zeta}\\ \frac{\partial z}{\partial \xi} & \frac{\partial z}{\partial \eta} & \frac{\partial z}{\partial \zeta}\end{bmatrix} \tag{11}$$

The enhanced part of the strain field $\boldsymbol{\varepsilon}^{\alpha}$, defined in the global coordinates (x,y,z), is computed according to:

$$\mathbf{G}=\frac{|\mathbf{J}_0|}{|\mathbf{J}|}\mathbf{F}_0^{-T}\mathbf{M}\,, \tag{12}$$

where $|\mathbf{J}|$ and $|\mathbf{J}_0|$ are the Jacobian determinant evaluated at the considered point in the element domain and in the center of the element respectively. In this equation, $\mathbf{F}_0$ denotes the 6x6 transformation matrix, expressed at the element center, already described by Andelfinger and Ramm [28]. It permits to transform the strain vector from the natural coordinates (ξ, η, ζ) to the global ones (x, y, z). **M** is the matrix containing the enhancing modes [28] which are expressed in the intrinsic coordinate system in a form which is independent of the element spatial configuration. Matrix **M** can be split in three parts:

$$\mathbf{M}=\begin{bmatrix}\mathbf{M}_1 & \mathbf{M}_2 & \mathbf{M}_3\end{bmatrix}, \tag{13}$$

with $\mathbf{M_1}$ grouping the linear terms:

$$\mathbf{M}_1=\begin{bmatrix}\xi & 0 & 0 & 0 & 0 & 0 & 0 & 0 & 0\\ 0 & \eta & 0 & 0 & 0 & 0 & 0 & 0 & 0\\ 0 & 0 & \zeta & 0 & 0 & 0 & 0 & 0 & 0\\ 0 & 0 & 0 & \xi & \eta & 0 & 0 & 0 & 0\\ 0 & 0 & 0 & 0 & 0 & \xi & \zeta & 0 & 0\\ 0 & 0 & 0 & 0 & 0 & 0 & 0 & \eta & \zeta\\ 25 & 26 & 27 & 28 & 29 & 30 & 31 & 32 & 33\end{bmatrix}, \tag{14}$$

while $\mathbf{M_2}$ contains the bilinear terms:

$$\mathbf{M}_2=\begin{bmatrix}0 & 0 & 0 & 0 & 0 & 0 & \xi\eta & \xi\zeta & 0 & 0 & 0 & 0 & 0 & 0 & 0\\ 0 & 0 & 0 & 0 & 0 & 0 & 0 & 0 & \xi\eta & \eta\zeta & 0 & 0 & 0 & 0 & 0\\ 0 & 0 & 0 & 0 & 0 & 0 & 0 & 0 & 0 & 0 & \xi\zeta & \eta\zeta & 0 & 0 & 0\\ \xi\zeta & \eta\zeta & 0 & 0 & 0 & 0 & 0 & 0 & 0 & 0 & 0 & 0 & \xi\eta & 0 & 0\\ 0 & 0 & \xi\eta & \eta\zeta & 0 & 0 & 0 & 0 & 0 & 0 & 0 & 0 & 0 & \xi\zeta & 0\\ 0 & 0 & 0 & 0 & \xi\eta & \xi\zeta & 0 & 0 & 0 & 0 & 0 & 0 & 0 & 0 & \eta\zeta\\ 34 & 35 & 36 & 37 & 38 & 39 & 40 & 41 & 42 & 43 & 44 & 45 & 46 & 47 & 48\end{bmatrix}, \tag{15}$$

and, finally, the trilinear terms are included in $\mathbf{M_3}$:

$$\mathbf{M}_3 = \begin{bmatrix} \xi\eta\zeta & 0 & 0 & 0 & 0 & 0 \\ 0 & \xi\eta\zeta & 0 & 0 & 0 & 0 \\ 0 & 0 & \xi\eta\zeta & 0 & 0 & 0 \\ 0 & 0 & 0 & \xi\eta\zeta & 0 & 0 \\ 0 & 0 & 0 & 0 & \xi\eta\zeta & 0 \\ 0 & 0 & 0 & 0 & 0 & \xi\eta\zeta \\ 49 & 50 & 51 & 52 & 53 & 54 \end{bmatrix} \tag{16}$$

In sub-matrices (14), (15) and (16) , the modes having non-zero terms in the three upper rows are related to the enhancement of the normal strain components and are therefore contributing to the treatment of the volumetric issue. Conversely, the modes with non-zero terms in the three lower rows correspond to shear strains and are used to solve shear locking.

The 30 EAS modes, corresponding to the 30 columns of (13) are selected to enhance the strain fields (9) up to a complete trilinear function in ξ, η and ζ and to be linearly independent from the 24 compatible strain modes included in the strain-displacement matrix **B**:

$$\mathbf{G} \cap \mathbf{B} = \varnothing \tag{17}$$

For instance, the first EAS mode in (14) corresponds to a linear variation of the strain component $\varepsilon_{\xi\xi}$ along the first axis (ξ), and, similarly, the effect of each EAS modes on the element's strain field can be identified. This effect differs from one mode to another which is proved by Andelfinger and Ramm in [28], who also showed that the EAS modes of the third sub-group $\mathbf{M_3}$ in equation (16) lead to no significant improvement on the overall element performance. Thus, in order to reduce the computational cost, these six modes are generally not used.

As presented by Simo and Rifai [3], once the **B** and **G** matrices have been obtained, the internal forces for the displacement dofs **U** and the residual for the EAS dofs $\boldsymbol{\alpha}$ can be written, in the element domain Ω_e, under the following expressions:

$$\mathbf{R}^{\mathrm{u}} = \int_{\Omega_e} \mathbf{B}^{\mathrm{T}} \boldsymbol{\sigma}^{\mathrm{m}} \mathrm{dV} \tag{18}$$

$$\mathbf{R}^{\alpha} = \int_{\Omega_e} \mathbf{G}^{\mathrm{T}} \boldsymbol{\sigma}^{\mathrm{m}} \mathrm{dV} \tag{19}$$

These integrals (18) and (19) are calculated numerically as follows:

$$\mathbf{R}^{\mathrm{u}} = \sum_{ipi=1}^{Npi} \mathbf{B}^{\mathrm{T}}(\xi,\eta,\zeta)_{ipi} \boldsymbol{\sigma}^{\mathrm{m}}{}_{ipi} \left|\mathbf{J}\right|_{ipi} \mathrm{W}_{ipi} \tag{20}$$

$$\mathbf{R}^{\alpha} = \sum_{ipi=1}^{Npi} \mathbf{G}^{\mathrm{T}}(\xi,\eta,\zeta)_{ipi} \boldsymbol{\sigma}^{\mathrm{m}}{}_{ipi} \left|\mathbf{J}\right|_{ipi} \mathrm{W}_{ipi} \tag{21}$$

Where $\left|\mathbf{J}\right|_{ipi}$ and W_{ipi} are the determinant of the Jacobian matrix (11) and the weights at the Gauss points. To fulfill the equation of the variational principle (1), the residual $\mathbf{R}^{\alpha}$ should be equal to zero while $\mathbf{R}^{\mathrm{u}}$ represents the internal forces of the element which should be in equilibrium with the externally applied forced (whose virtual work is included in $\pi_{\mathrm{ext}}(\eta)$).

The linearization for the displacement **U** and the EAS modes $\boldsymbol{\alpha}$ leads to the following system of equations at the element level:

$$\begin{bmatrix} \mathbf{K}^{\mathrm{uu}} & \mathbf{K}^{\mathrm{u}\alpha} \\ \mathbf{K}^{\alpha\mathrm{u}} & \mathbf{K}^{\alpha\alpha} \end{bmatrix} \begin{Bmatrix} \Delta\mathbf{U} \\ \Delta\boldsymbol{\alpha} \end{Bmatrix} = \begin{bmatrix} \mathbf{F}_{\mathrm{ext}} - \mathbf{R}^{\mathrm{u}} \\ -\mathbf{R}^{\alpha} \end{bmatrix} \tag{22}$$

with:

$$\mathbf{K}^{\mathrm{uu}} = \frac{\partial \mathbf{R}^{\mathrm{u}}}{\partial \mathbf{U}},\ \mathbf{K}^{\alpha\mathrm{u}} = \frac{\partial \mathbf{R}^{\alpha}}{\partial \mathbf{U}},\ \mathbf{K}^{\mathrm{u}\alpha} = \frac{\partial \mathbf{R}^{\mathrm{u}}}{\partial \boldsymbol{\alpha}} \text{ and } \mathbf{K}^{\alpha\alpha} = \frac{\partial \mathbf{R}^{\alpha}}{\partial \boldsymbol{\alpha}} \tag{23}$$

Here, the exponents u and α denote the displacement-based and enhanced-based terms.

Since the finite element interpolation for the enhanced strain $\boldsymbol{\varepsilon}^{\alpha}$ is not connected across the element boundaries, the EAS modes can be eliminated at the element level by static condensation before assembling the element matrices to the global matrices. By solving the second equation in (22), the increment of the additional dofs $\Delta\boldsymbol{\alpha}$ yields, at element level, to the following form:

$$\Delta\boldsymbol{\alpha}=-\left[\mathbf{K}^{\alpha\alpha}\right]^{-1}(\mathbf{R}^{\alpha}+\mathbf{K}^{\alpha u}\Delta\mathbf{U}) \tag{24}$$

Now, replacing $\Delta\boldsymbol{\alpha}$ by its expression in the first equation of the discrete linearized system of equations in (22), the global stiffness matrix and the force vectors can be written, at the element level, as:

$$\mathbf{K}^{\mathrm{EAS}}\Delta\mathbf{U}=\mathbf{F}_{\mathrm{ext}}-\mathbf{R}^{\mathrm{EAS}} \tag{25}$$

with the global element matrices:

$$\mathbf{K}^{\mathrm{EAS}}=\mathbf{K}^{uu}-\mathbf{K}^{u\alpha}(\mathbf{K}^{\alpha\alpha})^{-1}\mathbf{K}^{\alpha u} \tag{26}$$

$$\mathbf{R}^{\mathrm{EAS}}=\mathbf{R}^{u}-\mathbf{K}^{u\alpha}(\mathbf{K}^{\alpha\alpha})^{-1}\mathbf{R}^{\alpha} \tag{27}$$

The incremental displacement $\Delta\mathbf{U}$ can be calculated according to (25), and thus the displacement $\mathbf{U}$ can be updated. Subsequently the increment $\Delta\boldsymbol{\alpha}$ can be calculated with (24) using the incremental displacement $\Delta\mathbf{U}$ and then it will be used to update the EAS parameter $\boldsymbol{\alpha}$.

It should be noted here that $\mathbf{K}^{\mathrm{EAS}}$ and $\mathbf{R}^{\mathrm{EAS}}$ are calculated at the element level. The equations (26) and (27) must be assembled for all elements and solved globally and lead to the following forms:

$$\mathbf{K}_{\mathrm{G}}^{\mathrm{EAS}}=\mathop{\mathrm{A}}_{elem=1}^{\mathrm{nelem}}\mathbf{K}^{\mathrm{EAS}} \tag{28}$$

$$\mathbf{R}_{\mathrm{G}}^{\mathrm{EAS}}=\mathop{\mathrm{A}}_{elem=1}^{\mathrm{nelem}}\mathbf{R}^{\mathrm{EAS}} \tag{29}$$

with A representing the finite element assembling operator.

2.3 Integration schemes

An important characteristic of a finite element is the numerical integration scheme. It consists in the number and the location of the integration points inside the element and it can have a significant influence on its mechanical behavior. For instance, the reduced integration or the selective reduced integration schemes are often used to avoid volumetric locking issues for hexahedral elements with an isochoric or nearly isochoric material behavior.

Despite their efficiency in term of locking treatment and computational time, reduced integration schemes have certain drawbacks such as the rank deficiency of the stiffness matrix, which can lead to no solution at all, or erroneous solutions in (25); thereby to the element instability which is known as 'hourglass effect'.

In the development of a solid-shell element dedicated to the modeling of thin-walled structures, an improved integration scheme with a large number of integration points along the thickness direction was considered. It is indeed expected that a high gradient of stress and strain along the thickness direction is present during the deformation of thin materials (during e.g. a bending deformation mode). The classical full integration of brick elements (with two integration points along each direction) is not able to accurately capture such large gradients. In this respect, in the present formulations, the stress is computed along a user-defined number of integration points along the thickness direction (ζ axis), as shown in Figure 1.

Figure 1.RESS (a) and SSH3D (b) integration schemes with n Gauss points through the thickness direction.

For the in-plane computation, the RESS element uses a reduced integration scheme with only one Gauss point to improve its computational efficiency, while the SSH3D employs a full integration scheme with four Gauss points.

Comparing the two integration schemes proposed for RESS and SSH3D formulations, it can be expected that, in term of accuracy in bending situations the SSH3D element is better both in the cases of in and out of plane bending. In term of stability, no complex stabilization technique is required with the fully integrated element, which is not the case for the reduced integration. Despite these advantages, the use of the full integration scheme presents some drawbacks in terms of computational efficiency and treatment of locking pathologies.

2.4 The Assumed Natural Strain (ANS) method in SSH3D

Traditionally, in addition to the EAS method, several previous research works employ the well-known Assumed Natural Strain method (ANS) to overcome transverse shear locking.

The key idea of the method is to determine some selected strain components at certain sampling points (SP) and thereafter the resulting value are interpolated at the element's Gauss points (GP). To clarify, this procedure is described in details in Figure 2.

- Classical strain interpolation:

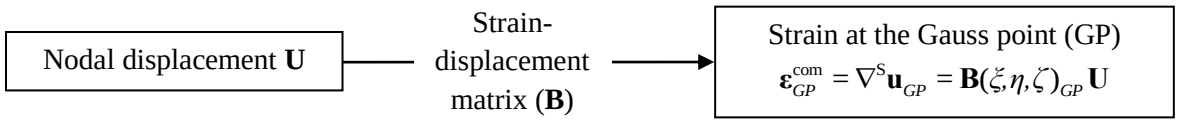

- ANS strain interpolation:

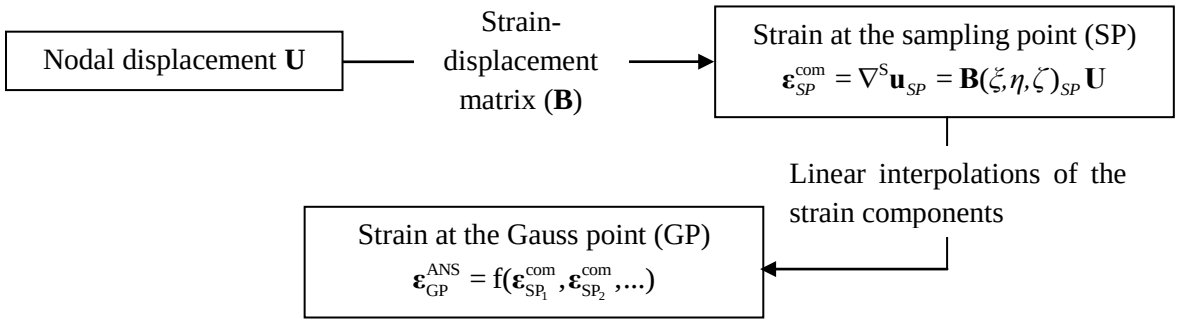

Figure 2. Interpolation of certain strain components in the ANS method.

In a general application of the ANS method, three parameters have to be determined, firstly the strain components to be replaced, then the number and position of the sampling points and finally the interpolation adopted for the independently assumed strains.

Different versions of the ANS method can be developed according to these choices (see Figure 3).

Due to its simplicity this method becomes very popular and used in several commercial codes in the improvement of the performance of 3D linear elements in the analysis of thin shell structures.

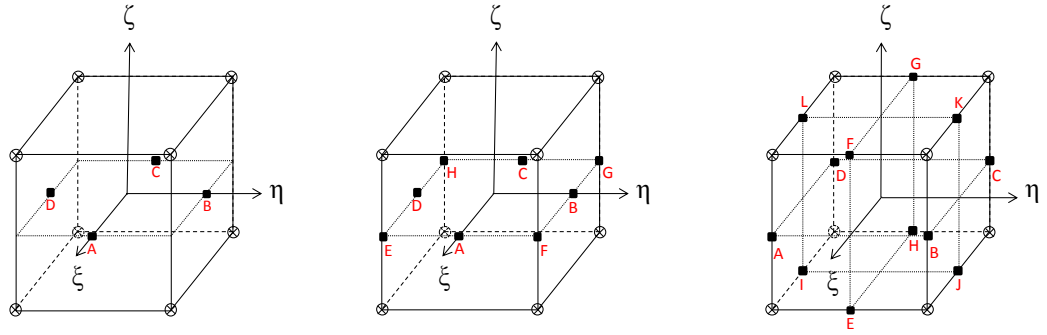

Figure 3. Number and location of the sampling points for different versions of the ANS method.

As introduced in Dvorkin and Bathe in [4], the first ANS approach (Figure 3 (a)) was dedicated to the treatment of transverse shear locking. Focusing on the transverse shear strain components, the sampling points are defined in isoparametric coordinates by A(1,0,0), B(0,1,0), C(-1,0,0) and D (0,-1,0). The modified (ANS) transverse shear strains are then determined by means of a linear interpolation of the compatible shear strains E_{13} and E_{23} evaluated at these sampling points (thanks to the classical **B**-matrix interpolation) and expressed in the natural coordinates:

$$2E_{13}^{ANS}=(1+\eta)E_{13}^{B}+(1-\eta)E_{13}^{D} \quad (30)$$

$$2E_{23}^{ANS}=(1-\xi)E_{23}^{A}+(1+\xi)E_{23}^{C} \quad (31)$$

According to (30) and (31), the transverse shear strains are assumed to be constant in ξ and linear in η direction for E_{13} and to be constant in η and linear in ξ direction for E_{23}. Several published works showed that this approximation is sufficient for thin structures [5, 6].

In Figure 3(b), a second version of the ANS interpolation is presented. For this version, the ANS technique is applied to transverse shear strains E_{13} and E_{23} to treat transverse shear locking. These strain components are obtained using the same interpolation functions already defined in (30) and (31).

In addition to the modifications on the interpolation of the transverse shear strains E_{13} and E_{23}, and similarly to the version proposed in [6, 23], a bilinear interpolation of the transverse normal strain sampled at the four corners E, F, G, H of the element mid-surface is applied to cure curvature thickness locking. The modified E_{33} component can be expressed as follows:

$$E_{33}^{ANS}=\frac{1}{4}\sum_{i=E,F,G,H}(1+\xi_i\xi)(1+\eta_i\eta)E_{33}^{i} \quad (32)$$

Where E_{33}^{i} is the classical transverse normal strain defined at the sampling point *i* located on the mid-surface of the solid element ($\zeta=0$). The coordinates of these sampling points are E (1,-1, 0), F (1,1,0), G (-1,1,0) and H(-1,-1,0).

The third approach of the ANS technique is presented in Figure 3(c), where all the modified strain components are interpolated with four sampling points. These sampling points are located at the corners of the three mid-surface corners ($\xi=0$, $\eta=0$ and $\zeta=0$). These components are interpolated in the natural axes system using the following functions:

$$E_{33}^{ANS}=\frac{1}{4}\sum_{i=A,B,C,D}(1+\xi_i\xi)(1+\eta_i\eta)E_{33}^{i} \quad (33)$$

$$E_{13}^{ANS} = \frac{1}{4} \sum_{i=I,J,K,L} (1+\eta_i \eta)(1+\zeta_i \zeta) E_{13}^{i} \tag{34}$$

$$E_{23}^{ANS} = \frac{1}{4} \sum_{i=E,F,G,H} (1+\xi_i \xi)(1+\zeta_i \zeta) E_{23}^{i} \tag{35}$$

It should be noted that for all ANS approaches presented above the remaining strain components are not modified.

Finally, it must be emphasized that the strain tensor **E** modified by the ANS technique has to be expressed in the (ξ,η,ζ) reference frame linked to the element (and not the global (x,y,z) frame). In the same way as the transformation used for the EAS technique (12), the transformation of the strain tensor from the isoparametric reference frame (ξ,η,ζ), noted **E**, to the global reference frame (x, y, z), noted **ε**, is adapted:

$$\boldsymbol{\varepsilon}^{ANS} = \frac{|\mathbf{J}_0|}{|\mathbf{J}|} . \mathbf{F}_0^{-T} . \mathbf{E}^{ANS} \tag{36}$$

With the combination of the EAS and ANS technique, the equation (9) becomes:

$$\boldsymbol{\varepsilon} = \boldsymbol{\varepsilon}^{ANS} + \boldsymbol{\varepsilon}^{\alpha} \tag{37}$$

Klinkel et al. [23] proved that the third ANS version using two planes and eight sampling points for the two modified transverse shear strains (as presented in Figure 3 (c)), does not lead to significant improvement with respect to the second version, when full integration is used. Therefore in some previous works describing fully integrated solid-shell elements using the ANS method (see e.g. the work of Hauptmann et al. [5], Vu-Quoc and Tan [6], Rah et al. [12]), only two sampling points per transverse shear strain component are usually taken into account. On the other hand, for reduced integrated solid-shell elements as presented in [9, 33, 41], based on numerical tests, these authors observed that the use of two sampling points may lead to non-physical zero eigenvalue of the element stiffness matrix and thus decrease the stability of the element. For this reason, four sampling points should be used for each transverse shear strain component.

In their current development, the SSH3D element implemented in LAGAMINE code can be used with the three ANS versions of Figure 3, while the RESS does not use the ANS method.

2.5 The stabilization technique in RESS

The integration scheme used for RESS finite element leads to a rank-deficiency of the formulation, coming exclusively from the reduced integration procedure in the element plane, as can be seen in Figure 1 (a). To reduce the occurrence of hourglass problems the physical stabilization procedure, originally suggested for a shell formulation [42], is extended to cover 3D solid elements.

The compatible strain tensor from displacement field ($\boldsymbol{\varepsilon}^{c}$) term, included in equation (9), can be rewritten into a convenient manner by the decomposed standard strain-displacement matrix **B**:

$$\boldsymbol{\varepsilon}^{c} = \left(\mathbf{B}^{c} + \mathbf{B}^{\xi}\xi + \mathbf{B}^{\eta}\eta + \mathbf{B}^{\zeta}\zeta + \mathbf{B}^{\xi\eta}\xi\eta + \mathbf{B}^{\xi\zeta}\xi\zeta + \mathbf{B}^{\eta\zeta}\eta\zeta\right)\mathbf{U} \tag{38}$$

Where **U** is the nodal displacements vector and the sub-terms of equation (38) are detailed in Alves de Sousa et al. [1]. In fact, for the special integration scheme (see Figure 1 (a)) where $\xi = 0$ and $\eta = 0$ for each integration point, the calculation of the strain-displacement matrix **B**, described in equation (13), turns out to be simply:

$$\mathbf{B} = \mathbf{B}^{c} + \mathbf{B}^{\zeta}\zeta \tag{39}$$

Under the in-plane reduced integration scheme adopted in this formulation, the constant c and ζ terms for the stabilization procedure are intentionally removed, since the used integration doesn't cancel them. The ζ term is not required due to the arbitrary number of integration points through the

thickness direction. For this reason, the strain-displacement sub-matrices that contribute to element stabilization and define the stabilization matrix ($\mathbf{B}^{\mathrm{H}}$) are:

$$\mathbf{B}^{\mathrm{H}} = \mathbf{B}^{\xi}\xi + \mathbf{B}^{\eta}\eta + \mathbf{B}^{\xi\eta}\xi\eta + \mathbf{B}^{\xi\zeta}\xi\zeta + \mathbf{B}^{\eta\zeta}\eta\zeta \tag{40}$$

Also, it is useful to decompose $\mathbf{B}^{\mathrm{H}}$ matrix by lines and to add a parameter in the formulation:

$$\begin{aligned}
\mathbf{B}^{\mathrm{H}}_{\xi\xi} &= \mathbf{B}^{\xi}_{\xi\xi}\xi + \mathbf{B}^{\eta}_{\xi\xi}\eta + \mathbf{B}^{\xi\eta}_{\xi\xi}\xi\eta + \mathbf{B}^{\xi\zeta}_{\xi\xi}\xi\zeta + \mathbf{B}^{\eta\zeta}_{\xi\xi}\eta\zeta \\
\mathbf{B}^{\mathrm{H}}_{\eta\eta} &= \mathbf{B}^{\xi}_{\eta\eta}\xi + \mathbf{B}^{\eta}_{\eta\eta}\eta + \mathbf{B}^{\xi\eta}_{\eta\eta}\xi\eta + \mathbf{B}^{\xi\zeta}_{\eta\eta}\xi\zeta + \mathbf{B}^{\eta\zeta}_{\eta\eta}\eta\zeta \\
\mathbf{B}^{\mathrm{H}}_{\zeta\zeta} &= \mathbf{B}^{\xi}_{\zeta\zeta}\xi + \mathbf{B}^{\eta}_{\zeta\zeta}\eta + \mathbf{B}^{\xi\eta}_{\zeta\zeta}\xi\eta + \mathbf{B}^{\xi\zeta}_{\zeta\zeta}\xi\zeta + \mathbf{B}^{\eta\zeta}_{\zeta\zeta}\eta\zeta \\
\mathbf{B}^{\mathrm{H}}_{\xi\eta} &= \mathbf{B}^{\xi}_{\xi\eta}\xi + \mathbf{B}^{\eta}_{\xi\eta}\eta + \mathbf{B}^{\xi\eta}_{\xi\eta}\xi\eta + \mathbf{B}^{\xi\zeta}_{\xi\eta}\xi\zeta + \mathbf{B}^{\eta\zeta}_{\xi\eta}\eta\zeta \\
\mathbf{B}^{\mathrm{H}}_{\xi\zeta} &= \beta\ \mathbf{B}^{\xi}_{\xi\zeta}\xi + \mathbf{B}^{\eta}_{\xi\zeta}\eta + \mathbf{B}^{\xi\eta}_{\xi\zeta}\xi\eta + \mathbf{B}^{\xi\zeta}_{\xi\zeta}\xi\zeta + \mathbf{B}^{\eta\zeta}_{\xi\zeta}\eta\zeta \\
\mathbf{B}^{\mathrm{H}}_{\eta\zeta} &= \beta\ \mathbf{B}^{\xi}_{\eta\zeta}\xi + \mathbf{B}^{\eta}_{\eta\zeta}\eta + \mathbf{B}^{\xi\eta}_{\eta\zeta}\xi\eta + \mathbf{B}^{\xi\zeta}_{\eta\zeta}\xi\zeta + \mathbf{B}^{\eta\zeta}_{\eta\zeta}\eta\zeta
\end{aligned} \tag{41}$$

Accordingly, when applying this formulation for thin-walled structures, the β parameter of equations (41) can be set to zero, not adding transverse shear energy and avoiding transverse shear locking [1]. Once the $\mathbf{B}^{\mathbf{H}}$ matrix is defined in natural frame, it is transformed to the global frame, applying the transformation matrix $\mathbf{F}_0^{-\mathrm{T}}$, similarly to equation (12):

$$\hat{\mathbf{B}}^{\mathrm{H}} = \mathbf{F}_0^{-\mathrm{T}}\mathbf{B}^{\mathrm{H}} \tag{42}$$

To avoid the volumetric locking phenomenon which occurs in solids finite elements, the B-bar approach is adopted as introduced by Malkus and Hughes [20]. Accordingly, the hourglass counterpart of the strain-displacement operator is divided into its volumetric (dilatational) and deviatoric components, the dilatational part being computed at the element centre:

$$\hat{\mathbf{B}}^{\mathrm{H}}(\xi,\eta,\zeta) = \hat{\mathbf{B}}^{\mathrm{H}}(\xi,\eta,\zeta)\big|_{\mathrm{dev}} + \hat{\mathbf{B}}^{\mathrm{H}}(0,0,0)\big|_{\mathrm{dil}} \tag{43}$$

Where $\hat{\mathbf{B}}^{\mathrm{H}}\big|_{\mathrm{dev}}$ and $\hat{\mathbf{B}}^{\mathrm{H}}\big|_{\mathrm{dil}}$ are further expanded according to equation (41).

Following an incremental-iterative Newton-Raphson scheme, both the stiffness matrix and the internal force vector on the equilibrium equations (25) must be corrected, resulting into a modified expression for nodal displacements calculation:

$$(\mathbf{K}^{\mathrm{EAS}} + \mathbf{K}^{\mathrm{H}})\Delta\mathbf{U} = \mathbf{F}_{\mathrm{ext}} - (\mathbf{R}^{\mathrm{EAS}} + \mathbf{R}^{\mathrm{H}}) \tag{44}$$

The following decomposition is considered for the hourglass stiffness $\mathbf{K}^{\mathrm{H}}$ and the increment of hourglass forces $\mathbf{R}^{\mathrm{H}}$:

$$\mathbf{K}^{\mathrm{H}} = \mathbf{K}^{\xi} + \mathbf{K}^{\eta} + \mathbf{K}^{\xi\eta} + \mathbf{K}^{\xi\zeta} + \mathbf{K}^{\eta\zeta} \tag{45}$$

$$\mathbf{R}^{\mathrm{H}} = \mathbf{R}^{\xi} + \mathbf{R}^{\eta} + \mathbf{R}^{\xi\eta} + \mathbf{R}^{\xi\zeta} + \mathbf{R}^{\eta\zeta} \tag{46}$$

Where the increment of hourglass forces ($\mathbf{R}^{\mathrm{H}}$) is calculated at the mid-step configuration as explained by Alves de Sousa et al. [1].

Each hourglass stiffness term of equation (45) is detailed below:

$$\mathbf{K}^{\xi} = \int_{\Omega}\left[\left(\mathbf{B}^{\xi}\right)^{\mathrm{T}}\mathbf{C}^{\mathrm{e}}\mathbf{B}^{\xi}\right]\xi^2\left|\mathbf{J}_0\right|\mathrm{d}V \tag{47}$$

$$\mathbf{K}^{\eta} = \int_{\Omega}\left[\left(\mathbf{B}^{\eta}\right)^{\mathrm{T}}\mathbf{C}^{\mathrm{e}}\mathbf{B}^{\eta}\right]\eta^2\left|\mathbf{J}_0\right|\mathrm{d}V \tag{48}$$

$$\mathbf{K}^{\xi\eta} = \int_{\Omega}\left[\left(\mathbf{B}^{\xi\eta}\right)^{\mathrm{T}}\mathbf{C}^{\mathrm{e}}\mathbf{B}^{\xi\eta}\right]\xi^2\eta^2\left|\mathbf{J}_0\right|\mathrm{d}V \tag{49}$$

$$\mathbf{K}^{\xi\zeta} = \int_{\Omega}\left[\left(\mathbf{B}^{\xi\zeta}\right)^{\mathrm{T}}\mathbf{C}^{\mathrm{e}}\mathbf{B}^{\xi\zeta}\right]\xi^2\zeta^2\left|\mathbf{J}_0\right|\mathrm{d}V \tag{50}$$

$$\mathbf{K}^{\eta\zeta} = \int_{\Omega}\left[\left(\mathbf{B}^{\eta\zeta}\right)^{\mathrm{T}}\mathbf{C}^{\mathrm{e}}\mathbf{B}^{\eta\zeta}\right]\eta^2\zeta^2\left|\mathbf{J}_0\right|\mathrm{d}V \tag{51}$$

Where the isoparametric domain is chosen such as $\int_\Omega dV = 8$ and $|\mathbf{J}_0|$, is the Jacobian determinant computed at the element centre.

Similarly, each hourglass force ($\mathbf{R}^H$) component of equation (46) is written as:

$$\mathbf{R}^{\xi} = \int_\Omega \left[\left(\mathbf{B}^{\xi} \right)^T \boldsymbol{\sigma}^{\xi} \right] \xi |\mathbf{J}_0| dV \tag{52}$$

$$\mathbf{R}^{\eta} = \int_\Omega \left[\left(\mathbf{B}^{\eta} \right)^T \boldsymbol{\sigma}^{\eta} \right] \eta |\mathbf{J}_0| dV \tag{53}$$

$$\mathbf{R}^{\xi\eta} = \int_\Omega \left[\left(\mathbf{B}^{\xi\eta} \right)^T \boldsymbol{\sigma}^{\xi\eta} \right] \xi\eta |\mathbf{J}_0| dV \tag{54}$$

$$\mathbf{R}^{\xi\zeta} = \int_\Omega \left[\left(\mathbf{B}^{\xi\zeta} \right)^T \boldsymbol{\sigma}^{\xi\zeta} \right] \xi\zeta |\mathbf{J}_0| dV \tag{55}$$

$$\mathbf{R}^{\eta\zeta} = \int_\Omega \left[\left(\mathbf{B}^{\eta\zeta} \right)^T \boldsymbol{\sigma}^{\eta\zeta} \right] \eta\zeta |\mathbf{J}_0| dV \tag{56}$$

The increments of the Cauchy stress $\boldsymbol{\sigma}$ are given as:

$$\boldsymbol{\sigma}^{\xi} = \xi \mathbf{C} \mathbf{B}^{\xi} \mathbf{U} \tag{57}$$

$$\boldsymbol{\sigma}^{\eta} = \eta \mathbf{C} \mathbf{B}^{\eta} \mathbf{U} \tag{58}$$

$$\boldsymbol{\sigma}^{\xi\eta} = \xi\eta \mathbf{C} \mathbf{B}^{\xi\eta} \mathbf{U} \tag{59}$$

$$\boldsymbol{\sigma}^{\xi\zeta} = \xi\zeta \mathbf{C} \mathbf{B}^{\xi\zeta} \mathbf{U} \tag{60}$$

$$\boldsymbol{\sigma}^{\eta\zeta} = \eta\zeta \mathbf{C} \mathbf{B}^{\eta\zeta} \mathbf{U} \tag{61}$$

Where $\mathbf{C}$ (6x6) is the constitutive stress-strain law tensor. In the set of equations (47) to (56), the non-constant terms can be calculated analytically:

$$\int_\Omega \xi^2 dV = \int_\Omega \eta^2 dV = \frac{8}{3} \tag{62}$$

$$\int_\Omega \xi^2 \eta^2 dV = \int_\Omega \xi^2 \zeta^2 dV = \int_\Omega \eta^2 \zeta^2 dV = \frac{8}{9} \tag{63}$$

It should be noted that no numerical integration is required at this stage, which results in saving a considerable computational time. More details on this solid-shell element formulation can be found in the published works of Alves de Sousa et al. [1, 2, 41].

2.6 Comparison between SSH3D and RESS formulations

To summarize the main features of the two developed formulations are listed in the following table:

Feature	SSH3D	RESS
EAS	User defined number of modes: from 1 to 30.	Only one EAS mode is implemented: Mode number 27 in (14).
ANS	Three ANS versions.	Not implemented.
Integration scheme	In plane four integration points with a user defined number of integration points through the thickness direction (from 2 to 10)	In plane reduced integration (1 point) with an arbitrary number of integration points through the thickness direction.
Stabilization	Not necessary	Stabilization technique using the method from the paper of Cardoso et al. [42].

Table 1. Features of the SSH3D and RESS solid-shell elements.

It should be noted that for both formulations it is essential that the element orientation is considered within the mesh generation, since the EAS, ANS techniques and the integration schemes described below depend on the element thickness direction.

3 Numerical applications

In this section, some numerical examples are selected to assess the accuracy and the efficiency of the developed elements in several situations. This section is divided into two main parts; in the first one, some simulations of linear elasticity problems cited in previous research works will be presented. Secondly, the performances of the present elements are evaluated in non linear elastoplastic cases using some sheet forming process simulations. In addition, the accuracy of SSH3D and RESS solid-shell elements is assessed in the prediction of springback phenomenon. In order to test the effect of the different techniques used to improve the performance of the solid-shell element SSH3D, numerical simulations were previously achieved with different sets of EAS modes and ANS versions. From these tests, we found out that the use of the second or the third ANS version (see Figure 3) leads almost to the same results. This observation agrees with the remark of Cardoso et al. [32] and Schwarze and Reese [10] concerning the use of a full integration scheme. Therefore, the second ANS version is used for SSH3D solid-shell element. In addition, despite the fact that the choice of the adequate EAS modes should strongly depend on the type of analysis and structure, it was found that the use of only 14 enhancing parameters leads to accurate results. The selected EAS parameters include the linear and bilinear modes used to enhance the membrane strains [E_{11}, E_{22}, $2E_{12}$] and the transverse normal strain E_{33} (i.e. 25 to 29, 34 and 35, 40 to 46) in the enhancing matrix (13). In contrast to certain optimal EAS solid-shell elements presented in the literature which can suffer from some locking pathologies since they are dedicated to the analysis of specific types of structures such as in Vu-Quoc and Tan [6] and Rah et al. [12] for the analysis of multilayer composites, the present SSH3D formulation with 14 EAS parameters can be used for the analysis of thin shell-like structures in several situations such as near incompressible cases e.g. elastoplastic analyses, highly distorted meshes and bending dominated problems. The RESS solid-shell formulation employs only one EAS parameter (mode 27 in (13)) to enhance the transverse normal strain E_{33} and an in-plane reduced integration scheme with and arbitrary number of integration points along the element thickness.

All obtained results are compared with experimental and numerical results published in previous research works and taken as reference solutions for the present formulations.

Through the following numerical tests, many finite element formulations were investigated for comparison purposes. Their main features are presented in Table 2 For the sake of brevity, the following abbreviations are employed:

Name	Description
HCiS12	Eight node fully integrated EAS element with 12 internal variables proposed in reference [25].
VQT7	Solid-shell element based on EAS concept with 7 EAS modes and ANS technique developed by Vu-Quoc and Tan [6].
S4E6P5	Degenerated four-node shell element presented by César de Sá et al.[43].

Table 2. Nomenclature for the tested solid-shell, solid and shell formulations.

3.1 Linear elastic problems

For elastic applications, since the stress distribution over the thickness is linear in bending situation, only two integration points through the thickness direction are sufficient. Therefore, in order to save computational time, two Gauss points are used for SSH3D in the following examples. While RESS employs three integration points through thickness (the minimum number as described in Alves de Sousa et al. [1].

3.1.1 Plate bending

This example is related to the analysis of a clamped square plate of dimension LxLxt with L= 100 and the thickness t = 1 or 0.1 (see Figure 4). The plate is subjected to a concentrated force F=16.367 at the center. It is considered as a classical shell example, hence it is presented in several research works (see [12, 25, 28]). The material parameters used for this example are an elasticity modulus E=10000 and Poisson's ratios ν=0.3 or 0.499. Owing to the symmetry of the problem, only one quarter of the plate is modeled with one layer of 2x2 or 4x4 solid-shell elements.

This test is used to exanimate the performance of the present formulations in the analysis of very thin plates under very critical conditions, i.e. high aspect ratios, coarse meshes and nearly incompressible material.

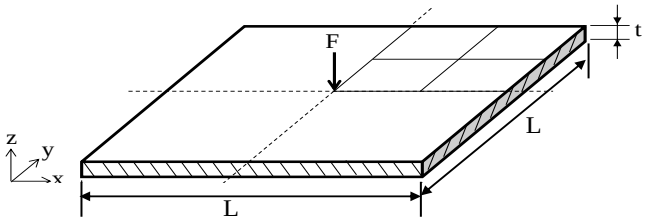

Figure 4. Clamped square plate with concentrated load

The theoretical deflection, which will be taken as a reference, is obtained thanks to Kirchoff plate theory according to the following relation:

$$W = 0.0056\frac{FL^2}{D} \tag{64}$$

Where D is the flexural rigidity of the plate which is obtained from Young's modulus E, Poisson's ratio ν and the plate thickness t as follows:

$$D = \frac{Et^3}{12(1-\nu^2)} \tag{65}$$

In Table 3, the numerical results of the present solid-shell formulations are normalized using the Kirchhoff plate solution and compared to other formulations from the literature for different Poisson's ratios, thicknesses and meshes.

ν	t/L	Mesh	RESS (UEL)	HCiS12	SSH3D	RESS
0.3	1/100	2x2	0.893	0.869	0.881	0.893
		4x4	0.978	0.970	0.973	0.979
	1/1000	2x2	0.886	0.866	0.869	0.891
		4x4	0.975	0.966	0.971	0.974
0.499	1/100	2x2	0.906	0.875	0.889	0.904
		4x4	0.984	0.973	0.978	0.982
	1/1000	2x2	0.896	0.868	0.883	0.900
		4x4	0.976	0.968	0.971	0.976

Table 3. Normalized transverse normal deflection of the clamped plate bending.

As shown in Table 3 the present solid-shell formulations provide good results even when material incompressibility is combined with high aspect ratio. This proves the excellent performance of SSH3D and RESS when volumetric and transverse shear locking can be an issue. On the other hand, it can be seen that the RESS element behaves slightly better than SSH3D. This can be explained by the fact that the use of in-plane reduced integration scheme is less sensitive to certain locking pathologies.

3.1.2 Cantilever plate out of plane bending

This example is performed to evaluate the out of plane bending behavior of the present formulations. It has been studied in numerous research works such as Simo et al. [44], Valente et al. [45], Vu-Quoc

et al. [6]. As depicted in Figure 5, the modeled structure consists in a cantilever plate of length L= 10, width w=1 and thickness t=0.1, fully clamped at one end and subjected to a pair point load F. The external load is increased up to a total force F= 40 . 10^3 t^3. Material parameters are a Young's modulus E=10^7 and to test the effect of the material incompressibility on the numerical prediction three Poisson's ratios were used ν=0, 0.3 and 0.499. In addition, to investigate the mesh refinement effect, the structure has been discretized into 10, 12 and 16 SSH3D and RESS solid-shell elements along its length direction and only one element on each of the two other directions.

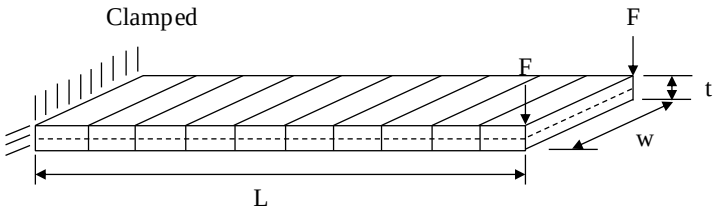

Figure 5. Out of plane cantilever beam - Geometry and boundary conditions.

For the three meshes and for a Poisson's ratio ν=0.3, Figure 6 compares the numerical results obtained by SSH3D and RESS elements with the theoretical solution according to the Timoshenko beam theory.

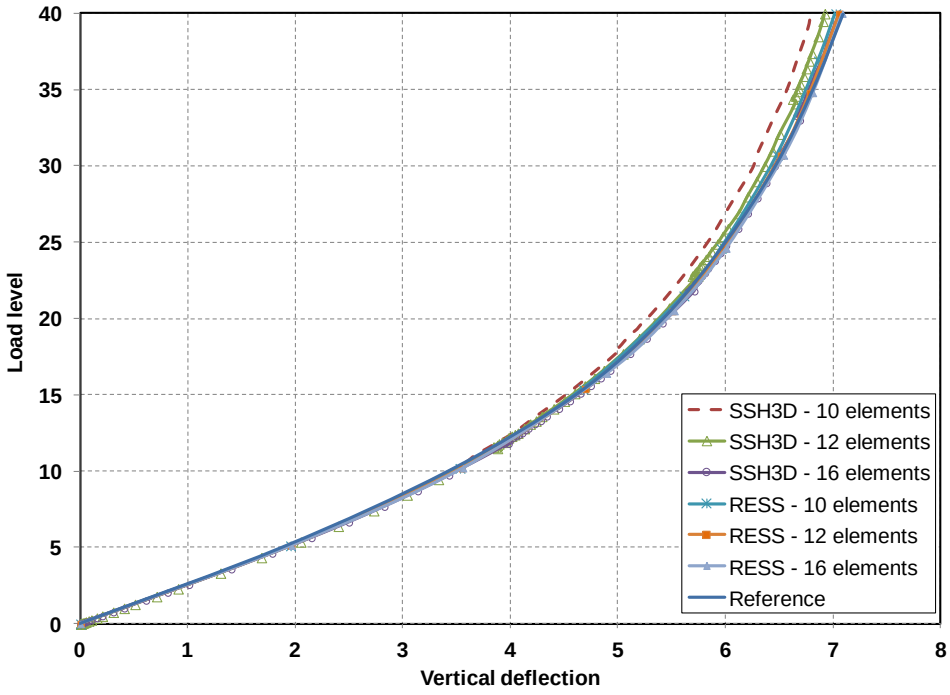

Figure 6. Out of plane cantilever beam - deflection values vs. load level - Poisson's ratio = 0.3.

This test was also used to investigate the sensitivity of the present solid-shell formulations to material incompressibility. To this end numerical analyses with 16x1x1 mesh and different Poisson's ratios were carried out. The results are presented in Figure 7.

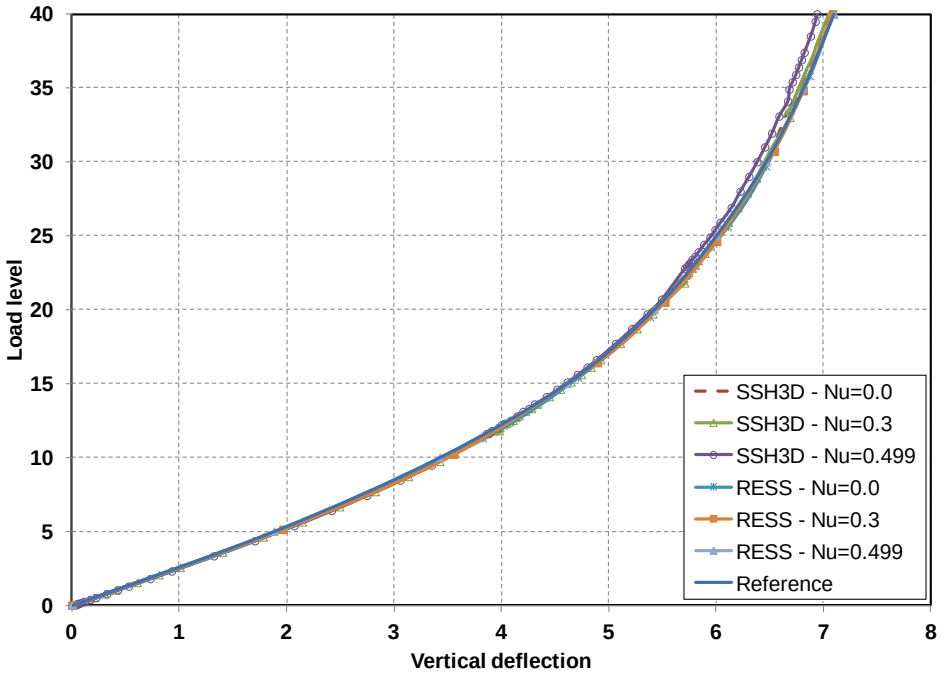

Figure 7. Out of plane cantilever beam - deflection values vs. load level - 16x1x1 mesh.

It can be seen that the proposed formulations are in good agreement with the reference solution for the three meshes with a slight improvement by using more elements along the plate length direction.

The results show also the excellent performance of the present formulations and their insensitivity for the various levels of Poisson's ratios.

It should be mentioned that the non-linearity observed in Figure 6 and Figure 7 comes from the large displacements encountered (geometric non linearity) rather than from material non linearity.

The remark of Vu-Quoc and Tan in [6] states that for flat plate undergoing small deformation, it is sufficient to consider the ANS treatment for only the transverse shear strain E_{13} and E_{23} (the additional ANS treatment for the transverse normal strain E_{33} being unnecessary). Accordingly, SSH3D element was tested with the first, the second and the third ANS versions (see Figure 3). In agreement with Vu-Quoc observations, it appeared that the modification of the normal strain component E_{33} by ANS did not influence the results. On the other hand, the SSH3D formulation without ANS method provided very poor results (with a final deflection w of 5.26) compared to the theoretical solution ($w \approx 7$). Hence we can conclude that the use of ANS method has a considerable influence for this test.

3.1.3 Cantilever beam in plane bending

This example is a very popular benchmark for geometrically nonlinear mixed finite element formulation, it was investigated in several published works (e.g. Simo et al. [46], Betsch et al. [29], Miehe [16] and Vu-Quoc and Tan [6]). This test is mainly used to evaluate the performance of the proposed solid-shell formulations in in-plane bending situation.

The geometry of the beam is characterized by a length of 1mm and a section of 0.1x0.1. The beam is clamped on one side and subjected to a transverse force F=1000 at the other side. Material properties considered are a Young's modulus $E=10^7$ and a Poisson's ratio $\nu=0.3$.

In order to evaluate the sensitivity of the present formulations to mesh distortion, the beam is modeled by ten solid-shell elements with two different meshes: the first is regular and the second is highly distorted as presented in Figure 8.

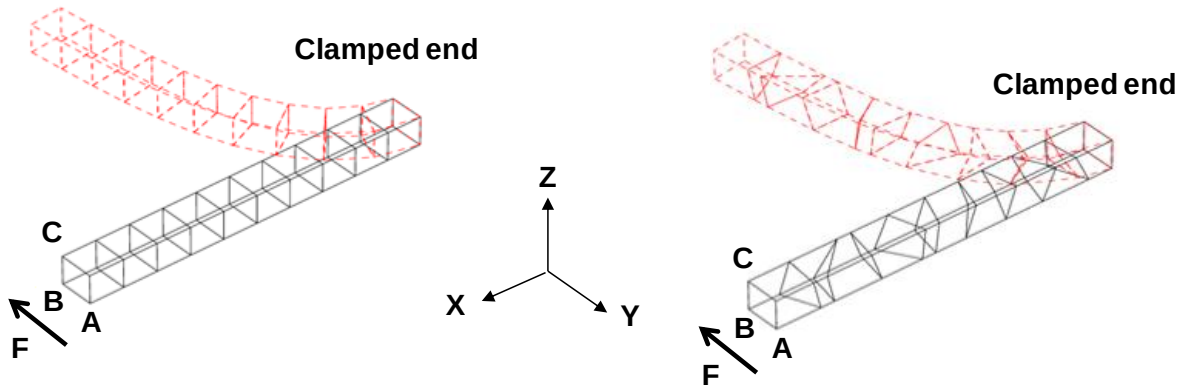

(a) (b)

Figure 8. In plane bending: deformed and undeformed regular (a) and distorted (b) meshes with 10 solid-shell elements.

The beam deflection curves obtained by SSH3D and RESS are plotted and compared to the solution presented by Vu-Quoc and Tan (VQT) [6] in Figure 9 and Figure 10 for the nodes A and B respectively.

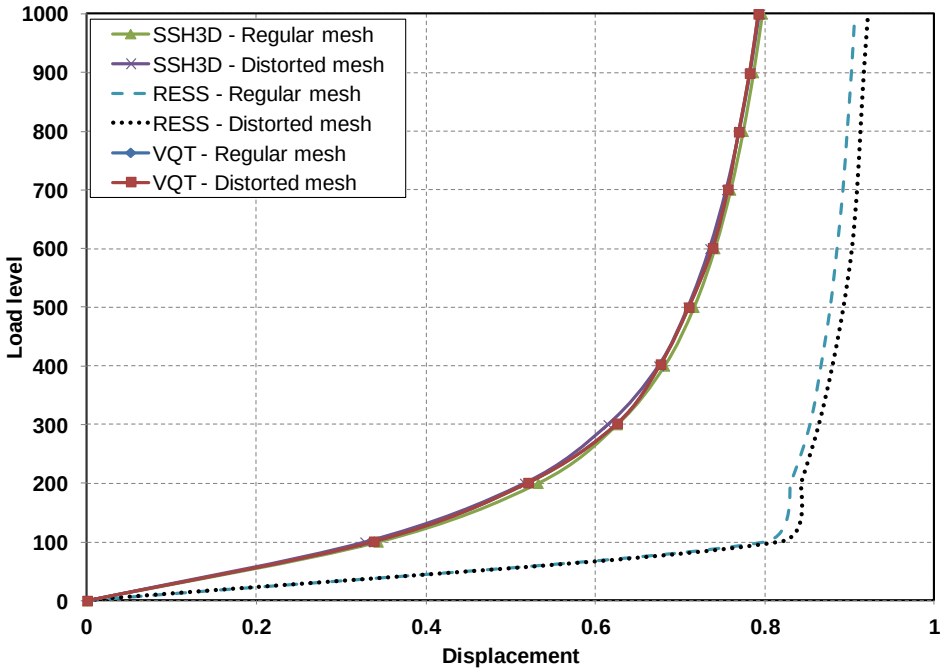

Figure 9. Cantilever beam in plane bending: point A, SSH3D and RESS results versus references [6].

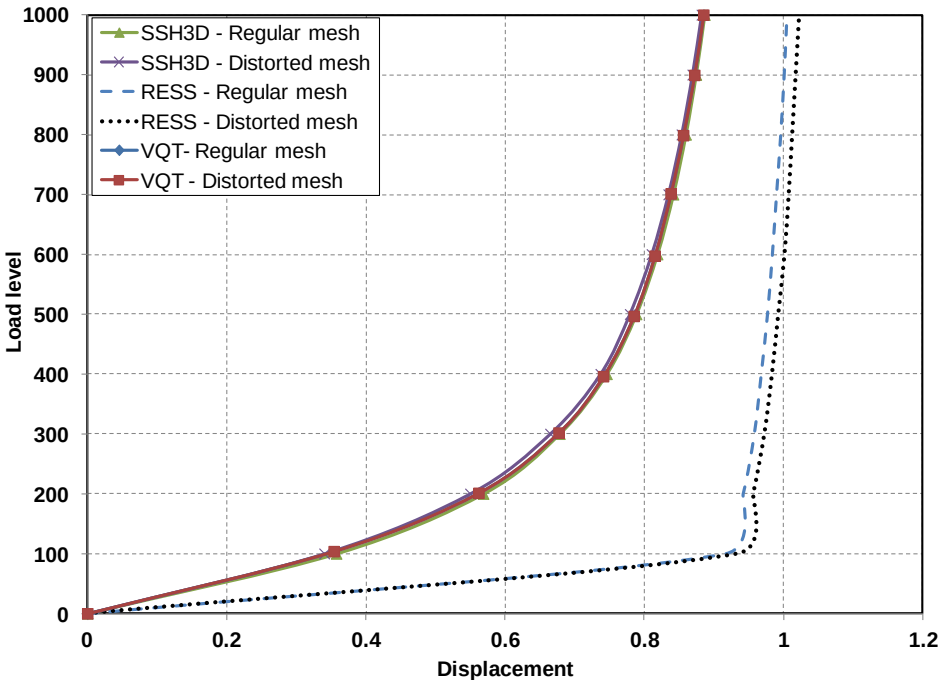

Figure 10. Cantilever beam in plane bending: point B, SSH3D and RESS results versus references [6].

It can be seen that the SSH3D and VQT7 formulations are superior to the RESS element for both regular and distorted mesh. This could have been expected since the RESS formulation uses an in-plane reduced integration scheme and the direction of the load is transversal. On the other hand, the proposed formulations show a high insensitivity to mesh distortions, and by comparing the SSH3D to the VQT (taken as reference), its good accuracy and performance are clearly demonstrated.
As discussed above the poor performance of RESS element is due to the fact that this formulation has the thickness as preferred direction. This can be clearly approved by the results depicted in Figure 11 and Figure 12 where the cantilever beam is bent in the element thickness direction.

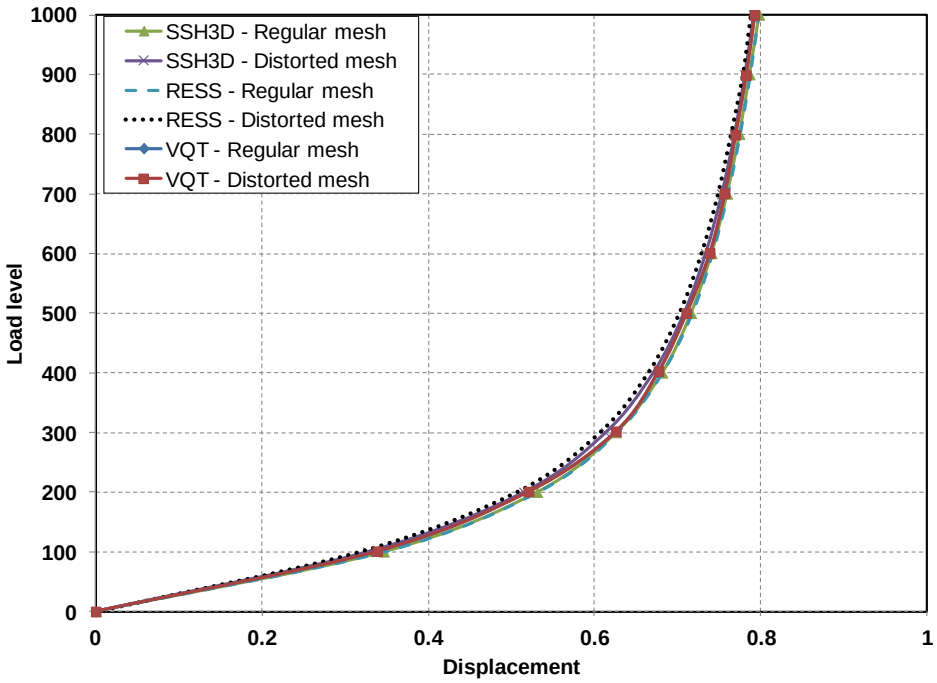

Figure 11. Cantilever beam: bending in Z direction - point B, SSH3D and RESS results versus references [6].

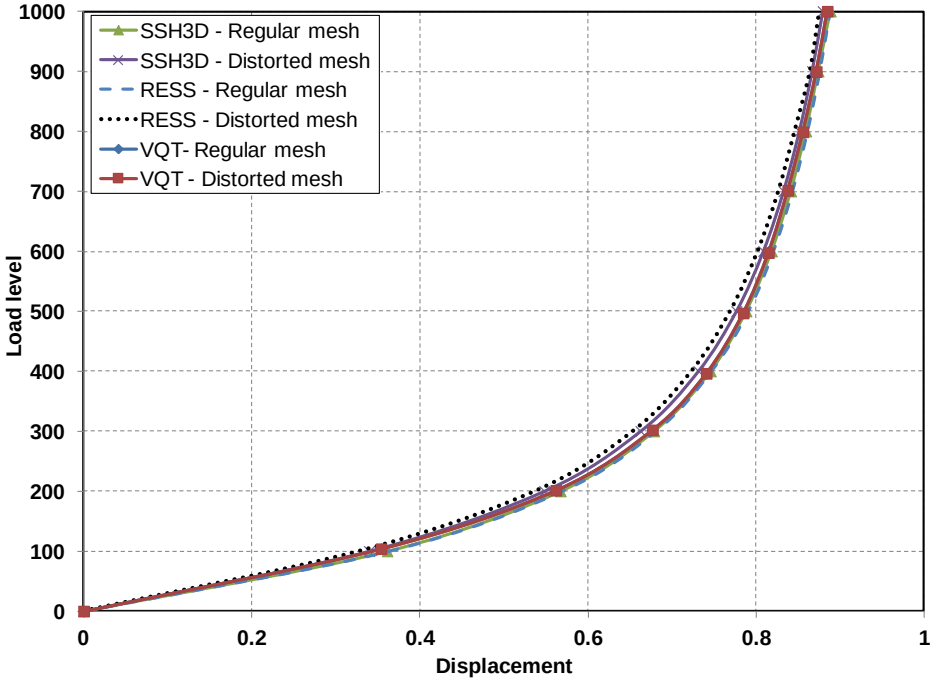

Figure 12. Cantilever beam: bending in Z direction - point C, SSH3D and RESS results versus references [6].

The above figures show the good performance and the insensitivity of both RESS and SSH3D solid-shell formulations when the cantilever beam bending is applied in the element thickness direction.

3.1.4 Pinched hemisphere with 18° hole

The pinched hemisphere with an 18° hole is a popular benchmark and one of the most stringent examples to test the behavior of the finite element formulation in geometrical non-linear domain due to its double curvature [6, 8, 10, 22, 47, 48]. As shown in Figure 13 the problem consists in a hemispherical shell with an 18° hole at the top subjected to concentrated forces, i.e. two equal and

opposite concentrated loads are applied in the x and y directions. Due to the double symmetry of the problem, the model includes only one quarter of the hemisphere meshed with 8x8 and 16x16 meshes of solid-shell elements. The material is linear elastic and its properties consist in a Young's modulus $E=6.825 \times 10^7$ and a Poisson's ratio $\nu=0.3$. The geometric parameters are the radius R=10 and the thickness t=0.04 of the shell. The hole at the top has a radius of 3.0902 since 18° in the meridional direction from the top is removed. Additional details on this problem can be found for instance in the work of Vu-Quoc [6].

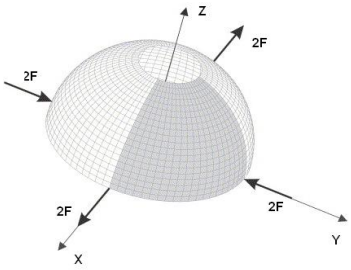

Figure 13. Pinched hemispherical shell with 18° hole.

The load is taken to increase up to the final value F=100.0. To assess the convergence behavior, the results are compared to shell elements presented in [22, 48].

The numerical results are plotted in Figure 14 and Figure 15 and compared to the solution published in the works of Valente et al. [48] to assess the performance and the convergence behavior of the present two solid-shell elements.

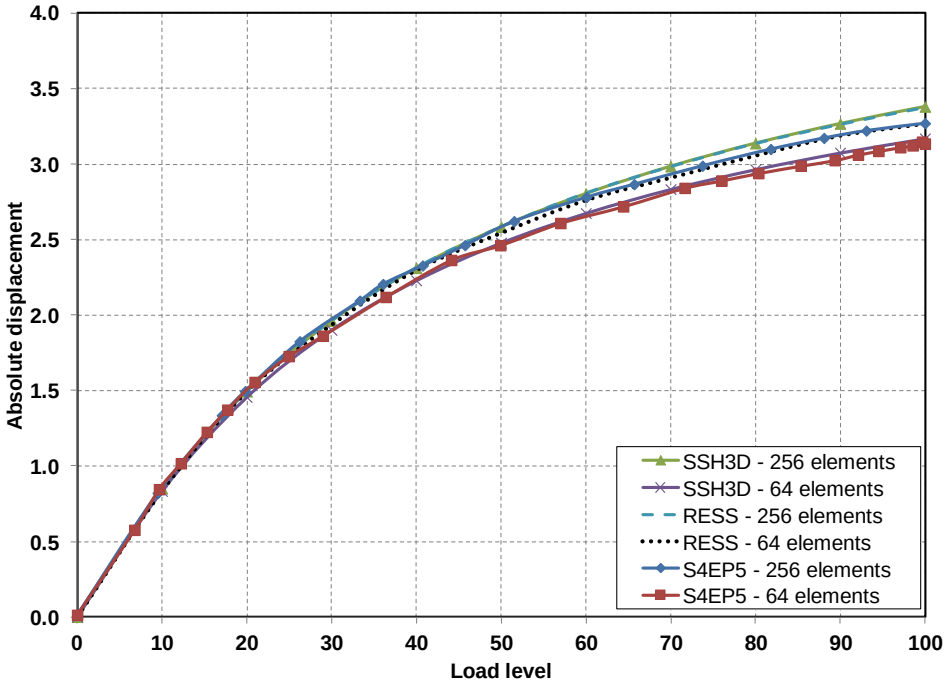

Figure 14. Pinched hemisphere with 18° hole: load – deflection diagram (along OX direction).

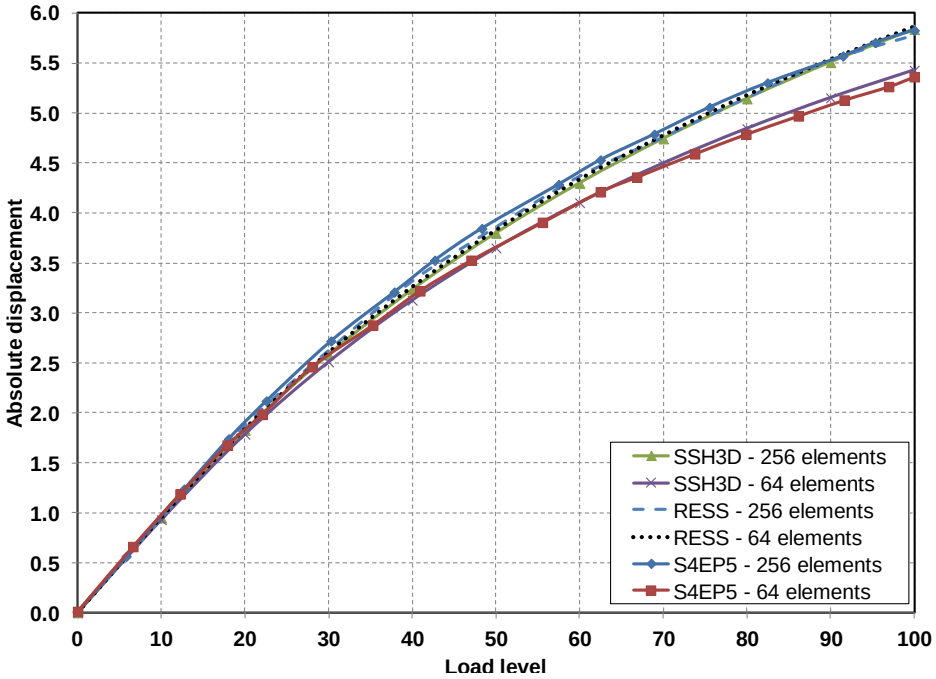

Figure 15. Pinched hemisphere with 18° hole: load – deflection diagram (along OY direction).

The results obtained by the proposed formulations are in good agreement with those provided by the reference. The mesh of 16x16 elements shows some improvement with respect to the results obtained with the 8x8 mesh. Besides, the SSH3D element is slightly stiffer than the RESS element which proves excellent performances for this test. These results show the good accuracy of the proposed solid-shell elements in modeling of structures with geometrical non-linearity.

3.2 Elastoplastic problems and springback prediction

In this section the performance of the proposed solid-shell elements are assessed in the analysis of sheet metal forming and springback predictions in presence of geometric, material and contact non-linearities. The present solid-shell elements SSH3D and RESS are characterized by their special integration schemes with an arbitrary number of integration points through the thickness direction. This characteristic makes it very competitive in the analysis of sheet metal forming problems involving strong non-linear through-thickness stress distribution. Therefore, in this section, the simulations carried out with the proposed elements use only one layer through the thickness with seven integration points to provide accurate solutions.

3.2.1 Hemispherical cup deep drawing

The hemispherical cup deep drawing is the benchmark test proposed at Numisheet 1999. According to the proceeding of Numisheet 1999 [49] the tools consist in a hemispherical punch of a diameter 100 mm ± 0.1 mm and a drawing die with an outer diameter of 220 mm ± 0.1 mm and an inner diameter (punch opening) of 102.4 mm ± 0.1 mm, the sheet thickness is 1.0 mm. More details on the geometrical dimensions are given in Figure 16. Benefiting from symmetry conditions, only a quarter of the model is analyzed. The sheet was modeled with a single layer of 752 solid-shell elements (see Figure 17). The tools (punch, die and blank-holder) are modeled as rigid bodies and discretized by triangle elements as shown in Figure 16. For each tool, one pilot node is associated to define the position of the tool and apply boundary conditions during the simulation. The analysis process consists in two phases. First, a constant blank holder force of 80 KN is applied during the simulation. This force creates an initial pressure distribution between blank-holder, blank and die. Once the blank

holder force is applied, the punch is moved to a total depth of 85 mm. During the process, the pilot node of the die remains fixed. In order to ensure the contact between the blank and the tools, contact elements are required. A Coulomb friction coefficient of 0.15 is used to define the contact. The blank is made of DDQ mild steel. The material properties are E= 2 x 10^5 MPa and ν=0.3 in elastic region; in the plastic range, the uniaxial stress strain curve is given by the swift's law:

$$\sigma = k(\varepsilon_0 + \varepsilon)^n \tag{66}$$

where k=557.11 MPa, n =0.2186 and ε_0=0.001562 are the hardening parameters. σ and ε are respectively the Cauchy stress and the natural strain (logarithmic strain) along the rolling direction of the sheet (taken as reference direction). The material anisotropic plasticity behavior is modeled by the Hill quadratic anisotropic yield criterion with the parameters F=0.655, G=0.771, H=1.222 and N=L=M=2.3844.

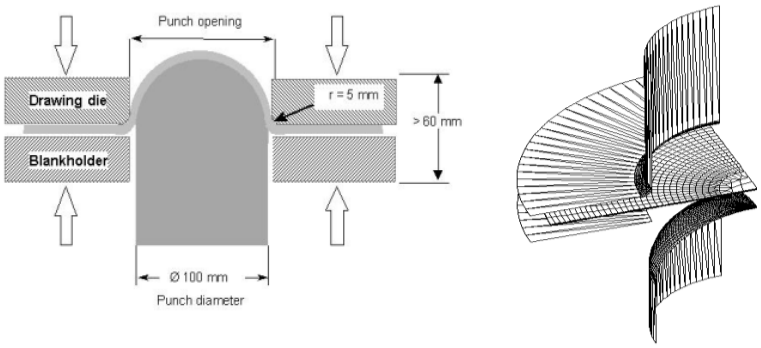

Figure 16. Hemispherical cup deep drawing: problem set-up, tools and FEM meshes

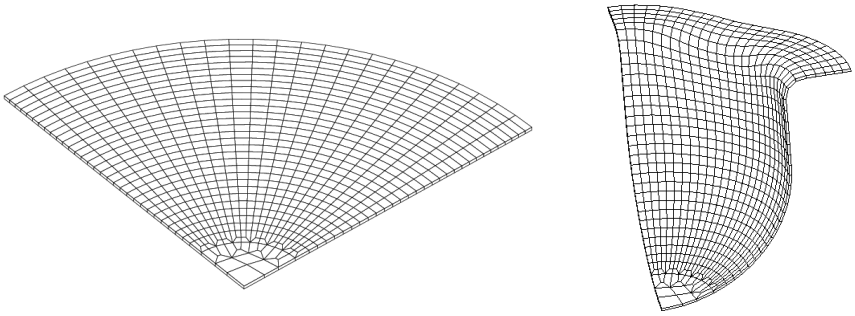

Figure 17. Hemispherical cup drawing: Initial and deformed meshes of the blank with one layer of 752 solid-shell elements.

In order to validate the proposed solid-shell element formulations, a comparison of the punch force-punch displacement curves predicted by numerical simulations with the experimental results (BE) reported in the proceeding of Numisheet 1999 [49] is depicted in Figure 18.

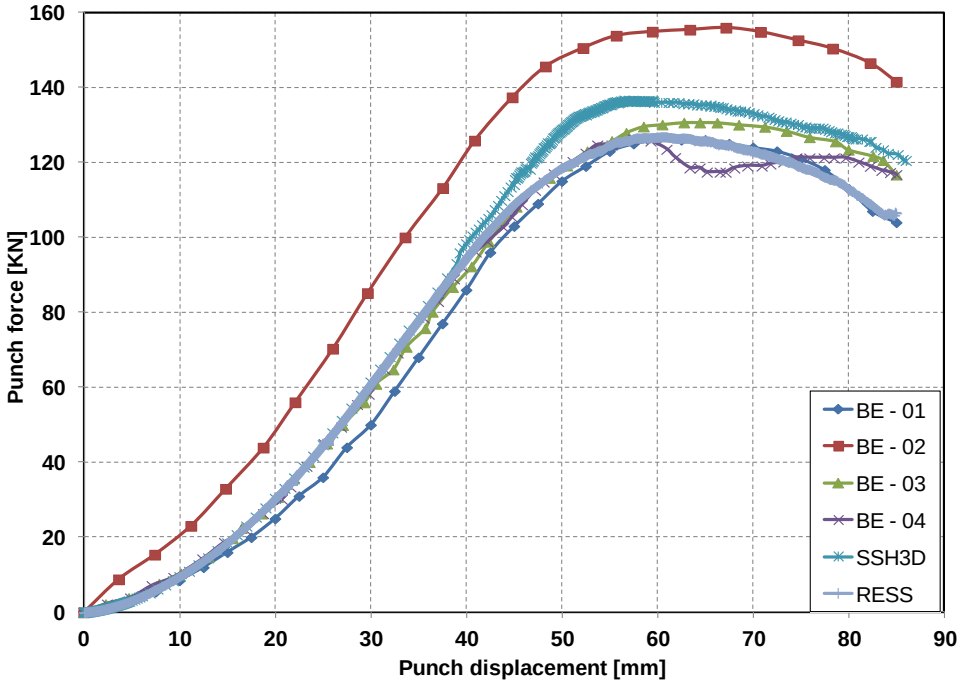

Figure 18. Punch force versus punch displacement curves for the hemispherical deep drawing.

In addition, Figure 19 compares the numerical predictions of the draw-in of the blank at the final punch displacement 85 mm as a function of the angle from the rolling direction using SSH3D and RESS solid-shell formulations with the experimental ones (BE-01, BE-02, BE-03 and BE-04).

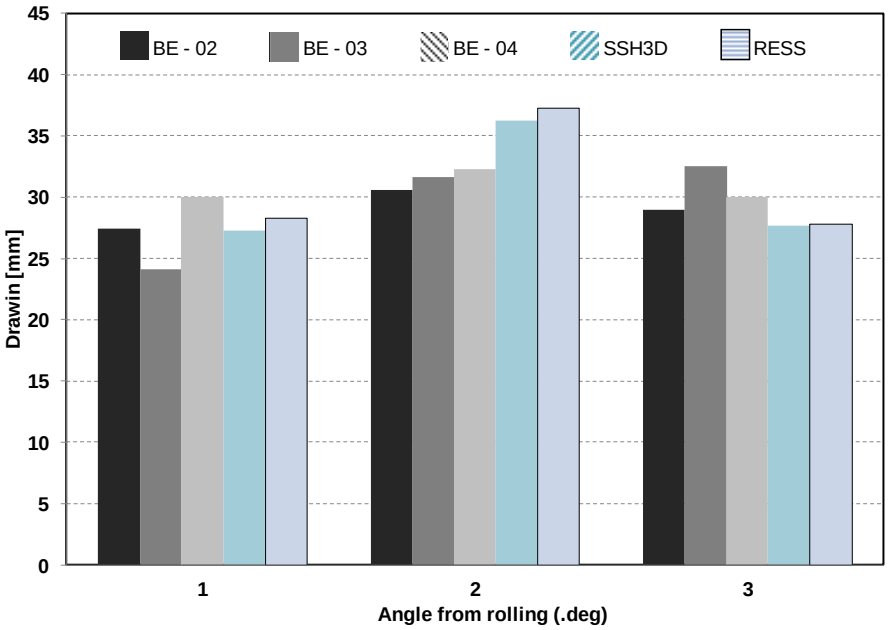

Figure 19. Draw-in in different angles from rolling at punch stroke = 85 mm

From Figure 18, it is possible to infer that the results provided by the SSH3D and RESS solid-shell elements are within the range of results obtained experimentally. Additionally, it can be seen in Figure 19 that the draw-in predicted by FE simulations show a good agreement with the ones measured experimentally with a small difference. This difference can be explained by the imprecision on the values of the friction coefficient, the blank-holder force or certain material parameters.

3.2.2 Springback analysis

In the previous example, the proposed solid-shell formulations showed a good performance; when sheet-metal forming is modeled without taking into account the unloading step. In this section, the unconstrained cylindrical bending test, which is one of the Numisheet 2002 benchmarks [50], is investigated to assess the performance of the proposed SSH3D and RESS solid-shell formulations in the prediction of the springback phenomenon. It has been considered in several previous research works [2, 10, 51-53] to evaluate the accuracy of some finite element formulations and constitutive models. The test is called "unconstrained" bending because of the absence of a blankholder.

In this study, two sheets with the same dimensions and made of High Strength Steel (HSS) and 6111-T4 Aluminum Alloy are considered. The material parameters are summarized in Table 4 and Table 7.

Owing to symmetry, only one quarter of the structure was modeled. The sheet consists in a rectangular blank of 120 mm of length, 30 mm of width and a thickness of 1 mm. As shown in Figure 20, in the sheet plane, the mesh is divided into three mesh zones with lengths of 17, 18, 25 mm discretized by 23, 15 and 10 elements respectively. Nine solid-shell elements are used along the width direction and only one element layer is considered with seven integration points through its thickness direction.

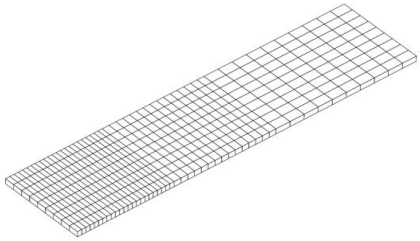

Figure 20. Finite element mesh with one layer of 432 elements.

- **Springback of unconstrained cylindrical bending (case 1)**

In this example, the sheet is made of High Strength Steel, which is described by mean of the von Mises plasticity and obeying the yield stress function of Swift type ($\sigma = k(\varepsilon_0 + \varepsilon)^n$) where the parameters are given in Table 4:

Elasticity		Hardening		
E (MPa)	ν	K (MPa)	ε_0	n
215980	0.3	620.19	0.005128	0.24557

Table 4. Blank material properties: Material parameters of HSS steel.

The interactions of the surfaces punch/sheet and die/sheet is defined by a coulomb friction coefficient μ=0.15.

As illustrated in Figure 21, the tools are composed of a cylindrical punch with a radius R1=23.5 mm and a die with a cavity radius R2=25 mm and a die-fillet radius R3=4mm.

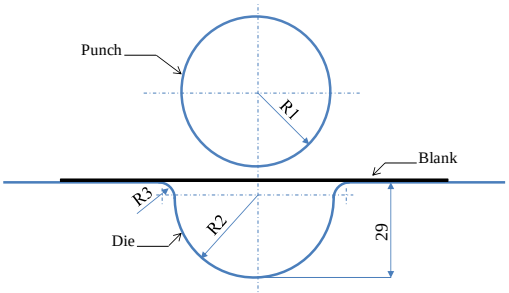

Figure 21. Tools for unconstrained bending process.

The springback is qualified by the angle ψ measured just after forming (at the maximum punch displacement) and at the end of the process (when the punch is removed). In addition, the angular distance between points of contact Φ is measured for different punch strokes to check the accuracy of the proposed formulations in predicting the forming behavior during the process (see Figure 22).

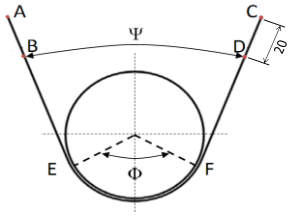

Figure 22. Definition of the angles for springback measurements.

In order to assess the accuracy of the present two solid-shell formulations SSH3D and RESS, the results obtained by numerical simulations are compared to experimental measurements (BE-01, BE-02, BE-03 and BE-04) reported in Numisheet 2002's benchmark [50] and the numerical results of RESS (UEL) presented in Alves de Sousa et al. [2].

The springback angle ψ measured from the deformed shape before (at the end of punch travel) and after springback (when the punch is removed) is given in Table 5 .

	High strength steel						
	Experiment [50]				Simulation		
	BE-01	BE-02	BE-03	BE-04	RESS (UEL) [2]	SSH3D	RESS
Before springback	22.77	22	23.02	20.86	23	22.73	23.01
After springback	37.42	35.67	30.90	35.36	37	33.54	33.89

Table 5. Springback angle ψ: comparison between experimental and numerical values

In addition, the angle Φ between the two punch-blank contact points which are the farthest from the centerline (see Figure 22) for different punch strokes is presented in Table 6:

	High strength steel						
	Experiment [50]				Simulation		
Punch stroke (mm)	BE-01	BE-02	BE-03	BE-04	RESS (UEL) [2]	SSH3D	RESS
7	22.58	20.47	46.81	32.15	36	29.94	30.04
14	61.91	61.89	89.91	76.09	74	76.09	46.18
21	111.29	107.50	133.43	123.79	126	125.17	123.07
28.5	157.73	150.60	180.71	161.02	164	159.86	168.45

Table 6. Angle Φ for different punch stroke: comparison between numerical and experimental results.

The evolution of the punch force predicted with the two proposed solid-shell elements are compared to the experimental results in Figure 23.

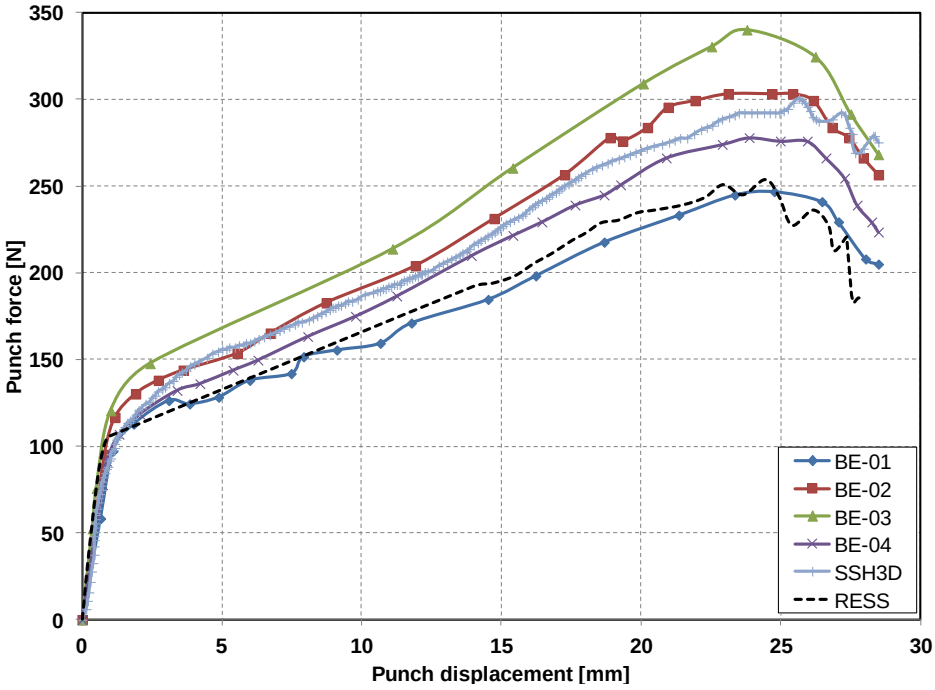

Figure 23. Unconstrained cylindrical bending: Punch force versus punch displacement

- **Springback of unconstrained cylindrical bending (case 2)**

As described in the work of Yoon et al [51], in this example the die geometry and dimensions are similar to those of the previous example but with a minor difference in the depth of the cavity (R2 is measured at the blank bottom surface). The new dimensions are illustrated in Figure 24.

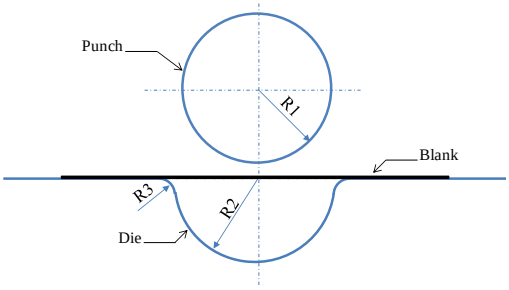

R1= 23.5 mm R2= 25 mm R3= 4 mm

Figure 24. Tools geometry for unconstrained cylindrical bending (modified version).

An isotropic model of von Mises with isotropic hardening was taking into account. The stress-strain curve is given by the following relation:

$$\sigma = A - B\exp(-c\varepsilon) \tag{67}$$

The material parameters for the 6111-T4 aluminum alloy are summarized in Table 7:

Elasticity		Hardening		
E (MPa)	ν	A (MPa)	B (MPa)	C
70 500	0.342	429.8	237.7	8.504

Table 7. Blank material properties: 6111-T4 aluminum alloy,

For this example, the springback angles ψ measured before and after springback are summarized in Table 8 and compared to the experimental measurements reported in Yoon et al. [51] and the numerical results predicted by RESS (UEL) presented in Alves de Sousa et al. [2].

	Aluminum alloy 6111-T4			
	Experiment	Simulation		
	Yoon et al. [51]	RESS (UEL) [2]	SSH3D	RESS
Before springback	35	37	38.52	38.22
After springback	68	67	68.16	71.37

Table 8. Springback angle: comparison between experimental and numerical values.

For the two springback analyses described above, it can be clearly seen the good concordance between the results measured experimentally and predicted by numerical simulations. This confirms the good performance and excellent accuracy of the proposed solid-shell elements SSH3D and RESS in predicting springback and analyzing bending-dominant problems with high non-linearities and complex contact constraints.

4 Conclusions

In this work two 3D solid-shell element formulations, namely SSH3D and RESS are presented. The main difference between these formulations is the number of Gauss points for the in-plane integration (full integration with four Gauss points for the SSH3D and reduced integration with only one point for the RESS). To assess the performance of these formulations, several numerical tests from the literature were simulated. The proposed elements have remarkable characteristics such as the use of multiple-point integration along the thickness which can more accurately describe the bending effect in sheet metal forming, especially when an elastoplastic material is used.

The comparison of the numerical results obtained with two different solid-shell formulations allowed us to highlight the drawbacks and advantages of each one with respect to the other. In addition, despite the computationally expensive calculation, the results show a remarkable increase in quality, and therefore also in efficiency compared to standard solid and shell elements.

In conclusion, the numerical examples show that very robust and excellent results can be achieved by the SSH3D and RESS formulations. In addition, their ability to accurately analyze sheet metal forming and springback even with only one element layer has been demonstrated. Compared to RESS, SSH3D solid-shell element is more general in the sense that it can behave better in different directions (not only the thickness direction) thanks to its in-plane full integration. It is also more versatile with regard to the various options proposed to the user. While for RESS, a relatively poor performance was shown in the shell plane (overestimated flexibility during in-plane bending). However, from a computational point of view, RESS is more efficient than SSH3D thanks to its in-plane reduced integration and the use of only one EAS mode.

Future targeted applications for the use of these solid-shell formulations are the modeling of the mechanical behavior of multilayer materials such as composite structures and coated metal sheets.

Generally, the optimal number of EAS parameters to alleviate locking pathologies are defined based on the type of analysis and can be obtained by numerical testing. In this purpose, an analysis of the efficiency of the EAS method using the framework of the subspace analysis is now underway and will be reported in future publications. This method was initially developed by César de Sà and Owen [54] for 2D elements and successfully applied later for 2D plane strain quadrilateral in [55, 56], shell elements [43, 48], 3D solid-shell elements by Alves de Sousa et al. [25] and Caseiro et al. [40].

5 Acknowledgements

As Research Director of the National Fund for Scientific Research, A.M. Habraken thanks this Belgian research fund for its support. The authors also acknowledge the Interuniversity Attraction Poles (IAP) Program P7/21 (Belgian Science Policy).

6 References

[1] Alves de Sousa RJ, Cardoso RPR, Valente RAF, Yoon JW, Gracio JJ, Jorge RMN, A new one-point quadrature enhanced assumed strain (EAS) solid-shell element with multiple integration points along thickness: Part I - geometrically linear applications, Int J Numer Meth Eng, 62 2005 952-977.

[2] Alves de Sousa RJ, Cardoso RPR, Valente RAF, Yoon JW, Gracio JJ, Jorge RMN, A new one-point quadrature enhanced assumed strain (EAS) solid-shell element with multiple integration points along thickness - Part II: Nonlinear applications, Int J Numer Meth Eng, 67 2006 160-188.

[3] Simo JC, Rifai MS, A Class of Mixed Assumed Strain Methods and the Method of Incompatible Modes, Int J Numer Meth Eng, 29 1990 1595-1638.

[4] Dvorkin EN, Bathe KJ, A continuum mechanics based four-node shell element for general nonlinear analysis., Engineering computations, 1 1984 77-88.

[5] Hauptmann R, Schweizerhof K, A systematic development of 'solid-shell' element formulations for linear and non-linear analyses employing only displacement degrees of freedom, Int J Numer Meth Eng, 42 1998 49-69.

[6] Vu-Quoc L, Tan XG, Optimal solid shells for non-linear analyses of multilayer composites. I. Statics, Comput Method Appl M, 192 2003 975-1016.

[7] Vu-Quoc L, Tan XG, Optimal solid shells for non-linear analyses of multilayer composites. II. Dynamics, Comput Method Appl M, 192 2003 1017-1059.

[8] Reese S, A large deformation solid-shell concept based on reduced integration with hourglass stabilization, Int J Numer Meth Eng, 69 2007 1671-1716.

[9] Schwarze M, Reese S, A reduced integration solid-shell finite element based on the EAS and the ANS concept-Geometrically linear problems, Int J Numer Meth Eng, 80 2009 1322-1355.

[10] Schwarze M, Reese S, A reduced integration solid-shell finite element based on the EAS and the ANS concept-Large deformation problems, Int J Numer Meth Eng, 85 2011 289-329.

[11] Abed-Meraim F, Combescure A, An improved assumed strain solid-shell element formulation with physical stabilization for geometric non-linear applications and elastic-plastic stability analysis, Int J Numer Meth Eng, 80 2009 1640-1686.

[12] Rah K, Paepegem WV, Habraken AM, Degrieck J, de Sousa RJA, Valente RAF, Optimal low-order fully integrated solid-shell elements, Comput Mech, 2012 1-18.

[13] Vu-Quoc L, Tan X, Efficient Hybrid-EAS solid element for accurate stress prediction in thick laminated beams, plates, and shells, Comput Method Appl M, 253 2013 337-355.

[14] Kaiping L, Cescotto S, An 8-node brick element with mixed formulation for large deformation analyses, Comput Method Appl M, 141 1997 157-204.

[15] Reese S, On a physically stabilized one point finite element formulation for three-dimensional finite elasto-plasticity, Comput Method Appl M, 194 2005 31.

[16] Miehe C, A theoretical and computational model for isotropic elastoplastic stress analysis in shells at large strains, Comput Method Appl M, 155 1998 193-233.

[17] Hauptmann R, Schweizerhof K, Doll S, Extension of the 'solid-shell' concept for application to large elastic and large elastoplastic deformations, Int J Numer Meth Eng, 49 2000 1121-1141.

[18] Klinkel S, Gruttmann F, Wagner W, A continuum based three-dimensional shell element for laminated structures, Comput Struct, 71 1999 43-62.

[19] Sze KY, Chan WK, Pian THH, An eight-node hybrid-stress solid-shell element for geometric non-linear analysis of elastic shells, Int J Numer Meth Eng, 55 2002 853-878.

[20] Malkus DS, Hughes TJR, Mixed finite element methods — Reduced and selective integration techniques: A unification of concepts, Comput Method Appl M, 15 1978 63-81.

[21] Hughes TJR, Generalization of selective integration procedures to anisotropic and nonlinear media, Int J Numer Meth Eng, 15 1980 1413-1418.

[22] Simo JC, Armero F, Geometrically non-linear enhanced strain mixed methods and the method of incompatible modes, Int J Numer Meth Eng, 33 1992 1413-1449.

[23] Klinkel S, Gruttmann F, Wagner W, A robust non-linear solid shell element based on a mixed variational formulation, Comput Method Appl M, 195 2006 179-201.

[24] Klinkel S, Wagner W, A geometrical non-linear brick element based on the EAS-method, Int J Numer Meth Eng, 40 1997 4529-4545.

[25] Alves de Sousa RJ, Jorge RMN, Valente RAF, César de Sa JMA, A new volumetric and shear locking-free 3D enhanced strain element, Engineering computations, 20 2003 896-925.

[26] Parente MPL, Valente RAF, Jorge RMN, Cardoso RPR, Alves de Sousa RJ, Sheet metal forming simulation using EAS solid-shell finite elements, Finite Elem Anal Des, 42 2006 1137-1149.

[27] Schwarze, M., Vladimirov, N. I, Reese, S., On the implementation of the EAS and ANS concept into a reduced integration continuum shell element and applications to sheet forming, International Journal of Material Forming, 2 2009 4.

[28] Andelfinger U, Ramm E, EAS-elements for two-dimensional, three-dimensional, plate and shell structures and their equivalence to HR-elements, Int J Numer Meth Eng, 36 1993 1311-1337.
[29] Betsch P, Gruttmann F, Stein E, A 4-node finite shell element for the implementation of general hyperelastic 3D-elasticity at finite strains, Comput Method Appl M, 130 1996 23.
[30] Bathe K-J, Dvorkin EN, A four-node plate bending element based on Mindlin/Reissner plate theory and a mixed interpolation, Chichester, United Kingdom: Wiley, 1985.
[31] Bischoff M, Ramm E, Shear deformable shell elements for large strains and rotations, Int J Numer Meth Eng, 40 1997 4427-4449.
[32] Cardoso RPR, Yoon JW, Mahardika M, Choudhry S, Alves de Sousa RJ, Valente RAF, Enhanced assumed strain (EAS) and assumed natural strain (ANS) methods for one-point quadrature solid-shell elements, Int J Numer Meth Eng, 75 2008 156-187.
[33] Norachan P, Suthasupradit S, Kim KD, A co-rotational 8-node degenerated thin-walled element with assumed natural strain and enhanced assumed strain, Finite Elem Anal Des, 50 2012 70-85.
[34] Cescotto S, Grober H, Calibration and Application of an elastic viscoplastic constitutive equation for steels in hot rolling conditions, Engineering Computations, 2 1985 101-106.
[35] Habraken AM, Cescotto S, An automatic remeshing technique for finite element simulation of forging processes, Int J Numer Meth Eng, 30 1990 1503-1525.
[36] S. Castagne, F. Pascon, G. Bles, A. M. Habraken, Developments in finite element simulations of continuous casting, Journal De Physique IV, 120 2004 447-455.
[37] Duchêne L, FEM study of metal sheets with a texture based, local description of the yield locus, PhD thesis, 2003, Department of Architecture, Geology, Environment and Constructions, University of Liège - Belgium.
[38] Henrard C, Numerical simulations of the single point incremental forming process, PhD thesis, 2008, Department of Architecture, Geology, Environment and Constructions, University of Liège - Belgium.
[39] Betsch P, Stein E, An assumed strain approach avoiding artificial thickness straining for a non-linear 4-node shell element, Commun Numer Meth En, 11 1995 899-909.
[40] J.F.Caseiro, R.J.AlvesdeSousa, R.A.F.Valente, A systematicdevelopmentofEASthree-dimensional finite elements for thealleviationoflockingphenomena, FiniteElementsinAnalysisandDesign, 73 2013 30-41.
[41] Alves de Sousa RJ, Yoon JW, Cardoso RPR, Valente RAF, Gracio JJ, On the use of a reduced enhanced solid-shell (RESS) element for sheet forming simulations, Int J Plasticity, 23 2007 490-515.
[42] Cardoso RPR, Yoon JW, Gracio JJ, Barlat F, de Sa JMAC, Development of a one point quadrature shell element for nonlinear applications with contact and anisotropy, Comput Method Appl M, 191 2002 5177-5206.
[43] César de Sá JMA, Jorge RMN, Valente RAF, Areias PMA, Development of shear locking-free shell elements using an enhanced assumed strain formulation, Int J Numer Meth Eng, 53 2002 1721-1750.
[44] Simo JC, Rifai MS, Fox DD, On a stress resultant geometrically exact shell model. IV, Variable thickness shells with through-the thickness stretching, United Kingdom: Elsevier, 1990.
[45] Valente RAF, Alves de Sousa RJ, Jorge RMN, An enhanced strain 3D element for large deformation elastoplastic thin-shell applications, Comput Mech, 34 2004 38-52.
[46] Simo JC, Fox DD, Rifai MS, On a stress resultant geometrically exact shell model. III, Computational aspects of the nonlinear theory, United Kingdom: Elsevier, 1990.
[47] Macneal RH, Harder RL, A proposed standard set of problems to test finite element accuracy, Amsterdam, Netherlands: Elsevier, 1985.
[48] Valente RAF, Jorge RMN, Cardoso RPR, César de Sá JMA, Grácio JJA, On the use of an enhanced transverse shear strain shell element for problems involving large rotations, Comput Mech, 30 2003 286-296.
[49] Gelin JC, Picart P, NUMISHEET '99: Proceedings of the 4th International Conference and Workshop on Numerical Simulation of 3D Sheet Forming Processes: BURS, 1999.
[50] Yang DY, NUMISHEET 2002: Proceedings of the 5th International Conference and Workshop on Numerical Simulation of 3D Shell Forming Processes -verification of Simulation with Experiment, 2002.
[51] Yoon JW, Pourboghrat F, Chung K, Yang DY, Springback prediction for sheet metal forming process using a 3D hybrid membrane/shell method, Int J Mech Sci, 44 2002 2133-2153.
[52] Salahouelhadj A, Abed-Meraim F, Chalal H, Balan T, Application of the continuum shell finite element SHB8PS to sheet forming simulation using an extended large strain anisotropic elastic–plastic formulation, Arch Appl Mech, 82 2012 1269-1290.
[53] Xu HJ, Liu YQ, Zhong W, Three-dimensional finite element simulation of medium thick plate metal forming and springback, Finite Elem Anal Des, 51 2012 49-58.
[54] César de Sá JMA, Owen, D.R.J, The imposition of the incompressibility constraint in finite elements - a review of methods with a new insight to the locking phenomenoa, Proc of the International Conference on Numerical Methods for Non-Linear Problems, Pineridge Press, editor, Swansea, UK, 1986.
[55] César de Sa JMA, Natal Jorge RM, New enhanced strain elements for incompressible problems, Int J Numer Meth Eng, 44 1999 229-248.

[56] César de Sá JMA, Areias PMA, Natal Jorge RM, Quadrilateral elements for the solution of elasto-plastic finite strain problems, Int J Numer Meth Eng, 51 2001 883-917.